JAMES | Journal of Advances in Modeling Earth Systems®

RESEARCH ARTICLE
10.1029/2024MS004380

Special Collection:
Development and applications of advanced urban models across scales

Improving Urban Climate Adaptation Modeling in the Community Earth System Model (CESM) Through Transient Urban Surface Albedo Representation

Yuan Sun[1,2], Bowen Fang[3], Keith W. Oleson[4], Lei Zhao[3,5,6], David O. Topping[1], David M. Schultz[1,2], and Zhonghua Zheng[1,2]

[1]Department of Earth and Environmental Sciences, The University of Manchester, Manchester, UK, [2]Centre for Crisis Studies and Mitigation, The University of Manchester, Manchester, UK, [3]Department of Civil and Environmental Engineering, University of Illinois Urbana-Champaign, Urbana, IL, USA, [4]Climate and Global Dynamics Laboratory, NSF National Center for Atmospheric Research, Boulder, CO, USA, [5]National Center for Supercomputing Applications, University of Illinois Urbana-Champaign, Urbana, IL, USA, [6]Institute for Sustainability, Energy, and Environment (iSEE), University of Illinois Urbana-Champaign, Urbana, IL, USA

Abstract Increasing the albedo of urban surfaces, through strategies like white roof installations, has emerged as a promising approach for urban climate adaptation. Yet, modeling these strategies on a large scale is limited by the use of static urban surface albedo representations in the Earth system models. In this study, we developed a new transient urban surface albedo scheme in the Community Earth System Model and evaluated evolving adaptation strategies under varying urban surface albedo configurations. Our simulations model a gradual increase in the urban surface albedo of roofs, impervious roads, and walls from 2015 to 2099 under the SSP3-7.0 scenario. Results highlight the cooling effects of roof albedo modifications, which reduce the annual-mean canopy urban heat island intensity from 0.8°C in 2015 to 0.2°C by 2099. Compared to high-density and medium-density urban areas, higher albedo configurations are more effective in cooling environments within tall building districts. Additionally, urban surface albedo changes lead to changes in building energy consumption, where high albedo results in more indoor heating usage in urban areas located beyond 30°N and 25°S. This scheme offers potential applications like simulating natural albedo variations across urban surfaces and enables the inclusion of other urban parameters, such as surface emissivity.

Plain Language Summary Higher albedo surfaces reflect more sunlight, which helps cool down cities. Yet, research into how altering the albedo of urban surfaces on a global scale can aid climate adaptation is limited. It either relies on empirical analysis, oversimplifying urban physical processes, or assumes that urban surface albedo remains constant over time. These limitations hinder our understanding of how changes in urban surfaces can impact the urban thermal environment. In this study, we developed a new option that allows urban surface albedo to vary over time within a global climate model. By gradually increasing global urban surface albedo, we quantified the cooling effects of implementing high urban albedo in a more realistic way. This new option sets the stage for future exploration of scenarios like painting roofs white or how materials age, shedding light on effective urban climate adaptation strategies.

Key Points:

- We developed a new representation scheme of transient urban surface albedo in Community Earth System Model (CESM) to improve urban climate adaptation modeling
- The new scheme enables CESM to assess evolving adaptation strategies for roofs, impervious roads, and walls over time
- Simulations show increasing roof albedo cools cities more effectively than increasing wall or impervious road albedo

Correspondence to:

Y. Sun and Z. Zheng,
yuan.sun-7@postgrad.manchester.ac.uk;
zhonghua.zheng@manchester.ac.uk

Citation:

Sun, Y., Fang, B., Oleson, K. W., Zhao, L., Topping, D. O., Schultz, D. M., & Zheng, Z. (2024). Improving urban climate adaptation modeling in the Community Earth System Model (CESM) through transient urban surface albedo representation. *Journal of Advances in Modeling Earth Systems*, *16*, e2024MS004380. https://doi.org/10.1029/2024MS004380

Received 1 APR 2024
Accepted 17 NOV 2024

Author Contributions:

Conceptualization: Zhonghua Zheng
Data curation: Yuan Sun, Zhonghua Zheng
Formal analysis: Yuan Sun, Zhonghua Zheng
Funding acquisition: Zhonghua Zheng
Investigation: Yuan Sun, Zhonghua Zheng

1. Introduction

Urban areas are often hotter than their surroundings and are increasingly vulnerable to extreme heat events (e.g., Krayenhoff et al., 2021; Tuholske et al., 2021; Zhao et al., 2014, 2021; Zheng et al., 2021). This heightened vulnerability is concerning because a 1°C temperature rise results in a 0.5%–8.5% potential increase in electricity demand (Santamouris et al., 2015) and 2%–5% increase in all-cause mortality (Yu et al., 2012). The escalating urban heat stress necessitates the need for effective cooling strategies as part of urban climate adaptation efforts (Djukic et al., 2016; Dursun & Yavas, 2015). Improving the urban thermal environment has become a focal point, with efforts to alter the built-up layout (e.g., Jamei et al., 2019; Zeng et al., 2023), morphological form (e.g., Liao et al., 2021), and biophysical properties, including surface roughness (e.g., H. Hou et al., 2023), emissivity (e.g., Chakraborty et al., 2021), and albedo (e.g., Liu et al., 2024). Among the array of adaptations through gray/physical infrastructure, using highly-reflective materials (Chen et al., 2019; Santamouris et al., 2011) and modifying coating color and texture (Senevirathne et al., 2021) have proven to be particularly effective. These

Methodology: Yuan Sun, Bowen Fang, Keith W. Oleson, Lei Zhao, David O. Topping, David M. Schultz, Zhonghua Zheng
Project administration: Yuan Sun, Zhonghua Zheng
Resources: Keith W. Oleson, Zhonghua Zheng
Software: Yuan Sun, Bowen Fang, Keith W. Oleson, Lei Zhao, Zhonghua Zheng
Supervision: Keith W. Oleson, Lei Zhao, David O. Topping, David M. Schultz, Zhonghua Zheng
Validation: Yuan Sun, Keith W. Oleson, Zhonghua Zheng
Visualization: Yuan Sun, Zhonghua Zheng
Writing – original draft: Yuan Sun, Zhonghua Zheng
Writing – review & editing: Yuan Sun, Bowen Fang, Keith W. Oleson, Lei Zhao, David O. Topping, David M. Schultz, Zhonghua Zheng

strategies reduce temperatures and mitigate urban heat island effects by altering the surface albedo of urban roofs and pavements (J. Yang et al., 2015).

Albedo refers to the ratio of reflected solar radiation to incoming solar radiation on surfaces. It influences local heat conditions by determining the amount of solar radiation that is absorbed versus reflected by these surfaces. Surfaces with higher albedo reflect more solar radiation and absorb less, resulting in cooler surface temperatures. To assess the cooling effects of managing urban surface albedo, a variety of methods have been developed, including statistical estimations (Akbari et al., 2009; Boriboonsomsin & Reza, 2007; Santamouris & Fiorito, 2021), physical-based experimentations (Lopez-Cabeza et al., 2022; Salvati et al., 2022), and multi-scale numerical simulations (Brousse et al., 2024; Krayenhoff et al., 2021). These investigations mainly focus on meso or micro-scale built environments, providing scientific evidence of changing albedo to deal with urban heat issues in certain cities. Besides concerning regional urban albedo effects, there is an emerging trend of implementing high albedo across regions, gradually shaping international networks such as C40 cities (https://www.c40.org/) for urban climate adaptation. So far, it remains challenging to quantify urban albedo impacts at a larger scale. Akbari et al. (2009) revealed that increasing horizontal surface albedo by 0.01 could increase global solar reflection by 1.27W m^{-2} and achieve an equivalency of 1.4kg m^{-2} CO_2 offset in urban areas. Xu et al. (2020) introduced that CO_2 equivalency by 0.01 pavement albedo changes ranges from 0.8 to 1.6kg m^{-2} when specifying meteorological attributes in 14 U.S. cities. However, these empirical studies are based on stationary climate conditions and oversimplify urban physical processes. To explicitly represent urban physical processes, several studies (Table 1) have employed process-based global climate models (GCMs) or Earth System Models (ESMs) to quantify albedo impacts under climate-change scenarios, such as the Community Earth System Model (CESM) (Oleson et al., 2010a; Zhang et al., 2016; Zhao et al., 2017), the University of Victoria Earth System Climate Model (UVic ESCM) (Akbari et al., 2012; Akbari & Matthews, 2012), and the global-regional Gas, Aerosol, Transport, Radiation, General Circulation, Mesoscale, and Ocean Model (GATOR-GCMOM) (Jacobson & Ten Hoeve, 2012). Compared to regional climate models, GCMs/ESMs have the advantage of simulating large-scale urban climate and interactions among all Earth system components, which provides insights into the broader context of global cooling effects and their spatial variability. For instance, using the Community Land Model-Urban (CLMU), Oleson et al. (2010a) demonstrated that installing white roofs (with a roof albedo of 0.9) across urban areas worldwide could result in a 33% decrease in the annual-mean canopy urban heat island intensity (CUHII). These studies provided scientific evidence for implementing large-scale urban high albedo as an adaptation strategy for the global warming trend.

Although previous studies using GCMs/ESMs explored the effects of high urban surface albedo, they fall short of adequately informing urban climate adaptation efforts. It is important to note that the fidelity of urban climate projections within these models is influenced by the representation and parameterization of urban areas (e.g., urban areas are much smaller than the grid-box size in the global models). Notably, most GCMs/ESMs do not include detailed urban modeling, which excludes the urban heat island effects in simulations (Zhao et al., 2021; Zheng et al., 2021). For GCMs/ESMs with urban models incorporated, the heterogeneity and complexity of urban density classes and surfaces are often simplified (Hertwig et al., 2021). Such simplification can introduce biases in urban climate simulations, consequently affecting the evaluation of adaptation strategies' effectiveness. For instance, simulations using the Catchment Land Surface Model (CLSM) with a high urban albedo value, where urban surfaces were not explicitly resolved, demonstrate a lack of resolution independence in their outputs of total radiation values (Menon et al., 2010). Moreover, studies apply static albedo parameters for simulations (Oleson et al., 2010a; Zhang et al., 2016), not considering any realistic implementation schedule for urban albedo changes. For instance, implementing high-albedo measures such as white-roof installations in urban areas is a gradual process, unlikely to be completed within a single day. Recognizing the dynamic nature of urban albedo changes is crucial for assessing the impact of such adaptations on urban climate resilience and planning effective strategies to mitigate urban heat island effects. This study leverages the state-of-the-art Earth system model, CESM, to simulate the phased introduction of high-albedo interventions in urban environments. We more realistically model the gradual adoption of urban high-albedo strategies and quantify their effects.

This paper is organized as follows. In Section 2, we outline CESM's urban representation and parameterization, highlighting our development of a transient urban albedo scheme. This new scheme is introduced as an alternative to the default scheme of static urban surface albedo. Section 3 presents the simulation results of continuously increasing albedo. Output analysis involves quantifying urban heat mitigation, urban surface energy changes, and

Table 1
Literature on Quantifying Effects of High Surface Albedo in Large-Scale Climate Models

Reference	Global climate model	Model component set	Atmospheric forcing	Simulation period	Simulation domain and grid spacing	Urban representation	Urban albedo changes	Effect quantification
Oleson et al. (2010a)	Community Climate System Model (CCSM)	Atmosphere–land coupled	Community Atmosphere Model version 3.5 (CAM3.5) outputs	1941–1999	Global, 1.9° latitude by 2.5° longitude	Explicit at the sub-grid level: roof, wall, and road	A step change in roof albedo from 0.32 to 0.9	Canopy urban heat island intensity (−33%), daily maximum temperature (−0.6°C), minimum temperature (−0.3°C)
Menon et al. (2010)	Goddard Earth Observing System Model Version 5 (GEOS-5)	Land-only	GSWP-2 data (Dirmeyer et al., 2006)	1984–1995	Global, 2° latitude by 2.5° longitude; continental US, 0.5° latitude by 0.5° longitude	Inexplicit: 0.7% of global surface areas	A step change in roof albedo by 0.25 and pavement albedo by 0.15	Global radiation forcing (1.63W m^{-2}), emitted CO_2 offset (57Gt)
Akbari and Matthews (2012)	University of Victoria Earth System Climate Model (UVic ESCM)	Fully coupled	Atmospheric model outputs	1800–2200	Unknown	Inexplicit: 1% of global surface areas	A step changes in land surface albedo by 0.05 or 0.1	Land surface temperature (−1.5K and −3K in 2200, respectively), emitted CO_2 offset (160Gt in 2200)
Akbari et al. (2012)	UVic ESCM	Fully coupled	Atmospheric model outputs	2010–2300	Unknown	Explicit at the grid level: urban areas	A step change in urban albedo by 0.1	Atmospheric temperature (−0.01°C–−0.07°C), emitted CO_2 offset (25Gt–150Gt)
Jacobson and Ten Hoeve (2012)	Gas, Aerosol, Transport, Radiation, General Circulation, Mesoscale, and Ocean Model (GATOR-GCMOM)	Fully coupled	Atmospheric model outputs	20 years	Global, 4° latitude by 5° longitude	Explicit at the grid level: roof and road	A step change in roof albedo from 0.12 to 0.65	Land air temperature (+0.07°C), urban air temperature (−0.02°C)
Zhang et al. (2016)	Community Earth System Model version 1.2.0 (CESM1.2.0)	Atmosphere–land coupled	CAM5 outputs	2010–2039	Global, 1.9° latitude by 2.5° longitude	Explicit at the sub-grid level: roof, wall, and road	A step change in roof albedo from 0.15 to 0.9	Canopy urban heat island intensity (−0.4°C)
Zhao et al. (2017)	CESM	Land-only	Data CAM outputs from fully coupled simulations	2071–2100	U.S. and southern Canada, 1.9° latitude by 2.5° longitude	Explicit at the sub-grid level: roof, wall, and road	A step change in roof albedo increase to 0.88	Surface urban heat island intensity (−3.4°C)

Note. An atmosphere–land coupled component set refers to a configuration in GCMs/ESMs where both the atmosphere and land components are active. A land-only set denotes that only the land component is active, with forcings from atmosphere data. A fully coupled set denotes a configuration where at least the ocean, atmosphere, and land components are active.

urban landunit and surface heterogeneity. Section 4 delves into the implications of our findings for urban climate-sensitive design, focusing on seasonal variations, spatial differences, and effects specific to different latitudes. Finally, Section 5 provides a summary of our conclusions and insights.

2. Methods and Data

This section describes the urban model in CESM (Section 2.1) and the new transient urban albedo scheme (Section 2.2). To examine the time-varying albedo functionality, we performed a series of simulations that vary urban albedo configuration (Section 2.3) with the corresponding model inputs (Section 2.4). We quantified albedo-induced changes based on the simulation outputs (Section 2.5).

2.1. Urban Representation and Parameterization

The land component of CESM2, known as the Community Land Model version 5 (CLM5) (Lawrence et al., 2019), represents land cover types using a “mosaic” sub-grid approach in which each landunit interacts with CAM separately (Schultz et al., 2016). There are five landunit types including natural vegetation, crop, lake, glacier, and urban. CLM5's urban model (CLMU) allows simulations of urban climate. In essence, CLMU classifies urban areas into density classes–tall building district (TBD), high density (HD), and medium density (MD)–and adopts Oke's “urban canyon” concept (Oke, 1987). The “urban canyon” delineates urban landunits into five surfaces: roof, sunlit wall, shaded wall, impervious, and pervious canyon floor. The CLMU technical description can be found in Oleson et al. (2010b) and Oleson and Feddema (2020), with Figure A1 illustrating the CLM5's representation hierarchy, the urban feedback to the atmospheric model, and the conceptualization of urban canyons and urban energy dynamics.

The single-layer urban canopy model of CLMU accounts for biophysical interactions between the atmosphere and urban canyon, where several biogeophysical modules calculate heat and water fluxes on each urban surface. The albedo of each urban surface directly affects reflected and absorbed solar radiation (see CESM source code file “UrbanAlbedoMod.F90”), with secondary effects on longwave and turbulent fluxes, and canyon air temperature. For instance, walls are distinguished as sun-walls and shade-walls with their individual radiative properties. Additionally, CLM5 integrates anthropogenic factors by incorporating a building energy model (Oleson & Feddema, 2020; Wang et al., 2023). This addition facilitates the simulation of indoor thermal conditions and heat exchanges, crucial for calculating the anthropogenic heat flux due to space heating and air conditioning.

In a CESM simulation, the initialization process starts with the “UrbanParamsType” module (Figure 1), which reads urban constant parameters from the land surface input data. These include eight urban albedo parameters: diffuse albedo and direct albedo for roof, wall, impervious road, and pervious road. Each albedo parameter is defined by four dimensions: the number of solar bands (“numrad”), the number of urban density types (“numurbl”), the latitude (“lsmlat”), and the longitude (“lsmlon”). That is, urban albedo parameters are spilt out into direct and diffuse albedos with visible and near-infrared wave bands. Once initialized, these parameters remain unchanged throughout the simulation. Thus, under the default scheme, modifying urban surface parameters such as albedo requires pausing the simulation, updating land surface data files, and initiating a new simulation case. This method, aimed at changing urban parameters statically, interrupts the workflow with interim outputs and results in extra time spent on output archiving, waiting in job queues, and the restarting process.

2.2. Implementation of the Transient Urban Albedo Scheme

We developed the “UrbanDynAlbMod”, a new module within CLM5, specifically designed for the transient urban albedo scheme (Figure 1). This module allows for dynamic modification of urban albedo parameters by adding a temporal dimension, permitting users to delineate albedo changes over specific time intervals, ranging from seconds to years. The scheme is focused on built surfaces including roofs, walls, and impervious roads.

The scheme provides three configurable options: “Dynamic_UrbanAlbedoRoof”, “Dynamic_UrbanAlbedoImproad”, and “Dynamic_UrbanAlbedoWall”. Users can tailor urban albedo modifications to their needs by enabling any of these options in the CLM5 namelist. For instance, activating “Dynamic_UrbanAlbedoWall = .true.” triggers the UrbanDynAlbMod, which then processes input data streams for variables such as DYN_ALBEDO_WALL_TBD, DYN_ALBEDO_WALL_HD, and DYN_ALBEDO_WALL_MD. These variables are defined

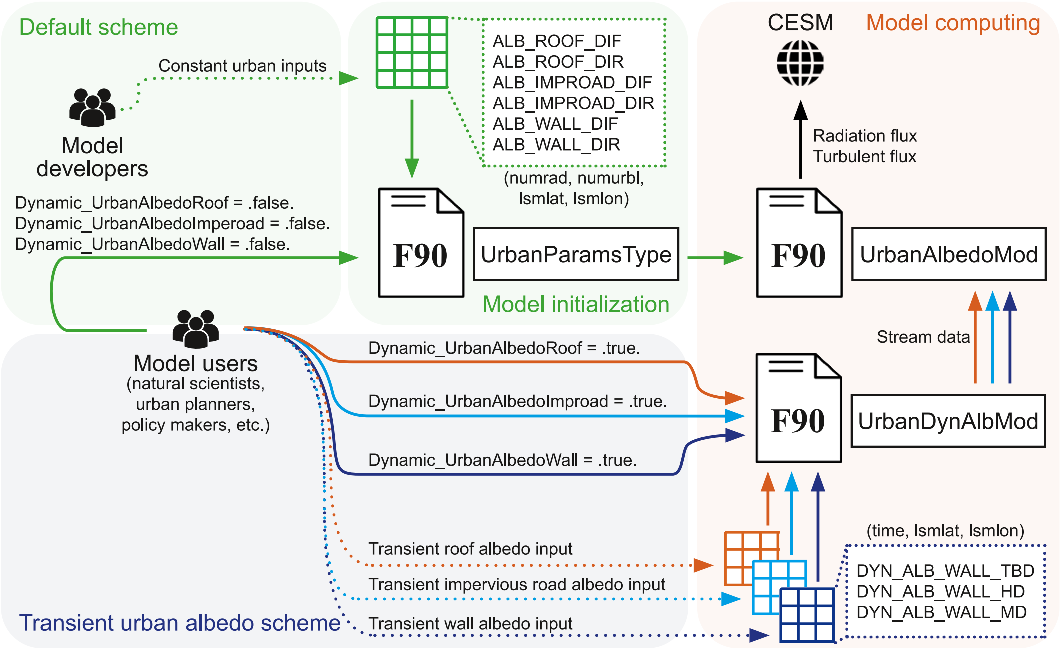

Figure 1. Workflow for implementing user-customized transient urban albedo. In the "UrbanParamsType" input data, the "numrad" dimension refers to the number of solar bands, encompassing both visible and near-infrared bands. The "numurbl" dimension refers to the number of urban density classes: TBD, HD, and MD. Dimensions "lsmlat" and "lsmlon" are land-masked latitude and longitude, respectively. For "UrbanDynAlbMod", the input data's "time" dimension signifies annual time steps for prescribed urban albedo modifications, complemented by "lsmlat" and "lsmlon" dimensions.

across three dimensions: time, "lsmlat", and "lsmlon", ensuring consistency in both diffuse and direct albedo values across the solar bands ("numrad"), similar to the handling of default constant parameters. The "UrbanDynAlbMod" then seamlessly incorporates these transient albedo parameters into the "UrbanAlbedoMod" for the computation of radiation and turbulent fluxes.

2.3. Experimental Design

We used CESM2.1.4 to assess urban climate adaptation strategies under varying urban albedo configurations with a grid spacing of 0.9375° latitude by 1.25° longitude. We executed CESM in a "land-only" component set, with an active CLM5, forced by atmospheric data. Simulations started with a 50-year spin-up driven by the satellite phenology (X. Li et al., 2022). After spin-up, the model reached a steady state, indicated by the evidence that globally averaged urban sensible heat flux and latent heat flux during the last 10 years were stable around 55.96 ± 0.38 and 35.45 ± 0.30W m^{-2}, respectively. Then, simulations ran over 85 years from 2015 to 2099 in the Shared Socioeconomic Pathways (SSPs) scenario SSP3-7.0 (Riahi et al., 2017). The SSP3-7.0 scenario outlines a future where limited action is taken to mitigate climate change or adapt to its impacts, leading to steadily increasing emissions and temperatures. This pathway projects CO_2 emissions to approximately double from current levels by 2100. Atmospheric forcing in this future scenario came from existing fully coupled simulations conducted by the National Center for Atmospheric Research (NCAR), based on the "BSSP370cmip6" (SSP370_CAM60_CLM50%BGC-CROP-CMIP6DECK_CICE%CMIP6_POP2%ECO%ABIO DIC_MOSART_CISM2%NOEVOLVE_WW3_BGC%BDRD) components set (available at https://docs.cesm.ucar.edu/models/cesm2/config/2.1.3/compsets.html). Note that the simulations from NCAR were submitted to the Coupled Model Intercomparison Project Phase 6 (CMIP6) for IPCC assessment. Additionally, this study did not consider urban land changes in the SSP3-7.0 scenario (Gao & O'Neill, 2020).

The control simulation (CNTL) acted as the baseline for comparison (Table 2). The ROOF_0.9 simulation applied a static roof albedo of 0.9, emulating the maximum reflectivity of a white roof. Note that both CNTL and

Table 2
Urban Climate Adaptation Strategies Under Varying Urban Albedo Configurations

Simulation name	Input data description	Roof albedo	Wall albedo	Impervious road albedo	Pervious surface albedo
CNTL	Static urban albedo	○	○	○	○
ROOF_0.9	Static high albedo of roof	0.9	○	○	○
ROOF_DA	Transient albedo of roof	■	○	○	○
WALL_DA	Transient albedo of wall	○	■	○	○
IMPROAD_DA	Transient albedo of impervious road	○	○	■	○
ROOF_IMPROAD_DA	Transient albedo of horizontal built surfaces	■	○	■	○
ROOF_IMPROAD_WALL_DA	Transient albedo of vertical and horizontal built surfaces	■	■	■	○

Note. The symbol ○ denotes static urban albedo parameters in CLM5, while ■ denotes transient urban surface albedo inputs. Albedo parameter values in each grid cell were modified to increase annually by 0.01 starting from 2015, capping at a maximum of 0.9. The albedo of pervious roads was not altered, in recognition of their natural characteristics.

ROOF_0.9 used the default scheme with static input data, aiming to replicate the earlier studies by Oleson et al. (2010a) and Zhang et al. (2016) but in a land-only component set. In contrast, the ROOF_DA simulation used the transient urban albedo scheme, incrementally increasing roof albedo by 0.01 (Akbari et al., 2012) annually since 2015, until reaching a maximum of 0.9, after which no further increases occurred. Similarly, the IMPROAD_DA and WALL_DA simulations implemented annual increases in impervious road albedo and wall albedos, respectively. The combined impacts of albedo modifications were further examined in ROOF_IMPROAD_DA and ROOF_IMPROAD_WALL_DA simulations, offering insights into the synergistic effects of varying albedo modifications on urban climate adaptation. The annual increment of 0.01 in the albedo of specific urban surfaces is an experimental assumption to model interventions. For example, in the ROOF_DA simulation, a 0.01 roof albedo increase per year raises the global mean urban surface albedo by 0.0044 per year, based on the assumption that roofs account for 44% of the urban surface. This rate is 10 times as high as the real-world urban surface albedo changes observed (0.0044 per decade) in 11 Chinese cities from 1986 to 2018 (Guo et al., 2022), which was attributed to multiple human activities including urban greening and conversion of natural surfaces into bright or dark built-up areas. In reality, the trend of global urban albedo changes is modest and generally downward. Ouyang et al. (2022) reported decreasing urban surface albedo alongside urbanization by converting croplands into urban lands. Wu et al. (2024) found that the downward urban albedo accelerated in recent decades, given that the annual-mean city-level albedo decreased rate during 2000–2020 was 0.0014 per year, twice as high as during 1986–2020. Compared to real-world observations, our assumptions of a 0.01 albedo increase rate on certain surfaces are far higher than the status quo, supposing intentional adaptation actions such as installing white roofs and applying high-reflective materials to accelerate urban albedo increase.

2.4. Land Surface Input Data

The default input data for urban land cover and urban parameters in CLMU are derived from the Jackson et al. (2010), which defined urban spatial extent according to population density using LandScan data representing the year 2004. The urban fractions are represented through the parameter PCT_URBAN (percent urban for each density type). As illustrated in Figures 2a–2c, the majority of urban areas, accounting for 79.0%, are classified as MD, while TBD and HD areas represent 0.1% and 20.9%, respectively. The PCT_URBAN parameter is constant, without considering urban land changes over time. Based on a categorization of global urban regions, Jackson et al. (2010) developed a set of constant global urban morphological, radiative, and thermal parameters for CLMU. The default configuration in CLMU standardizes urban albedo values for both direct and diffuse reflectance, maintaining consistent behavior across both visible and near-infrared bands. Figures 2d–2f illustrate the categorization of urban roof albedo constants in the default input data set, spanning 33 urban regions with three distinct urban density types.

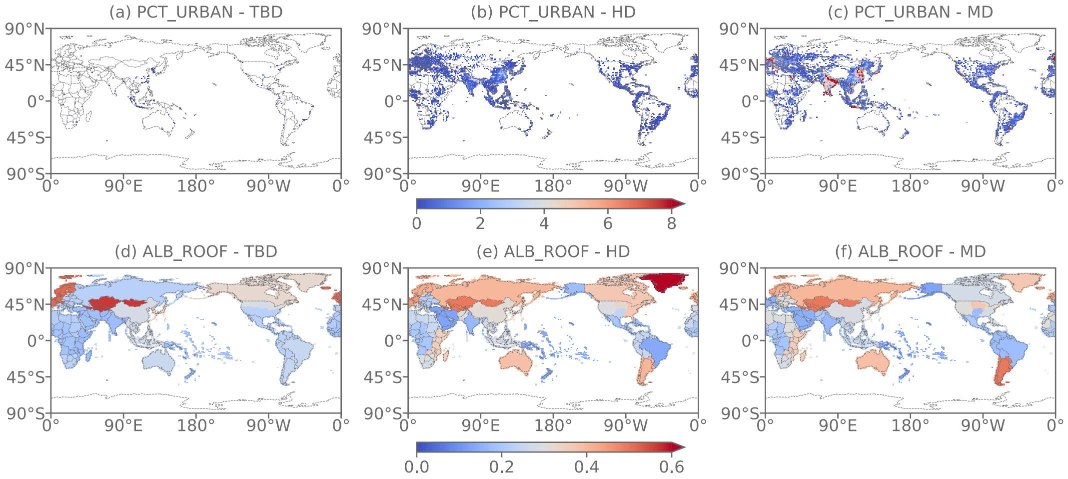

Figure 2. Spatial variations of prescribed and static urban fraction and roof albedo in the standard CESM land surface input data. (a)–(c) Percent of urban areas (%) in TBD, HD, and MD. (d)–(f) Roof albedo in TBD, HD, and MD. Both parameters come from raw data aggregated to 0.05° resolution (Oleson & Feddema, 2020).

Alongside the default input data set, a series of data sets featuring transient urban albedo values have been developed, each corresponding to the simulations outlined in Table 2. These data sets follow a hypothetical scenario where albedo is incrementally increased by 0.01 each year, reaching a cap of 0.9 (see Section 2.3).

2.5. Analysis of Effects Induced by Urban Surface Albedo Modifications

Previous studies have focused on the albedo cooling effects on urban surface temperature, 2-m air temperature, and indoor temperature, with further analysis on urban heat island intensity and the possibility of reducing air conditioning needs (J. Yang et al., 2015). The potential drawbacks of increased urban surface albedo, such as intensified thermal stress in the street canyons (Erell et al., 2014), and elevated heating demands during winter (Georgescu et al., 2014), have been acknowledged as well. Based on CESM simulations, we explored the implications for urban thermal environments, the urban energy budget, and urban landunit and surface heterogeneity. Our analysis spans three future periods as outlined by the IPCC (2023): the near-term (2021–2040), mid-term (2041–2060), and long-term (2081–2099), providing an insight into the impacts of urban albedo modifications.

2.5.1. Urban Thermal Environments

Urban thermal environments are assessed through several temperature indices, including global-mean urban heat island intensity, urban heat stress, and indoor air temperature (Section 3.1). Urban heat island is calculated by contrasting urban and rural temperatures, involving land surface temperature for surface urban heat island intensity (SUHII) and 2-m near-surface air temperature for canopy urban heat island intensity (CUHII). The SUHII and CUHII are calculated by:

$$\mathrm{SUHII} = \mathrm{TG\_U} - \mathrm{TG\_R}, \tag{1}$$

and

$$\mathrm{CUHII} = \mathrm{TSA\_U} - \mathrm{TSA\_R}, \tag{2}$$

where TG_U and TG_R are the surface temperatures in urban and rural areas, respectively, and TSA_U and TSA_R are the 2-m air temperatures in the urban and rural areas, respectively. TSA_R and TG_R come from fraction-weighted corresponding variables in vegetated and crop fractions. Details on calculating urban heat island intensity based on CESM outputs are described in Appendix B.

Urban heat stress is assessed by a set of human-related indices (Oleson et al., 2015), including the 2-m US National Weather Service Heat Index (NWS_HI) (Steadman, 1979), 2-m apparent temperature (AT) (Steadman, 1994), 2-m simplified wet-bulb globe temperature (sWBGT) (Willett & Sherwood, 2012), 2-m humidity index (HUMIDEX) (Masterton & Richardson, 1979), and 2-m discomfort index (DI) (Epstein & Moran, 2006). These five indices represent combinations of critical near-surface temperature, humidity, and/or wind conditions, beyond which adverse health effects are more likely to occur. Although all indices are measured in °C, they each apply different weightings to these environmental factors based on their respective impacts on human comfort. Each index is associated with specific thresholds for identifying potential health and comfort risks. Given the complexity of urban heat dynamics, relying on a single metric may not fully capture the full scope of heat stress. Therefore, we use multiple indices to account for the uncertainties surrounding heat stress and offer detailed assessments of critical threshold events. This multiple-index approach also allows for comparison with other studies using the same metrics, enhancing the robustness of our conclusions regarding the timing of critical threshold crossing and the effects of continuous albedo increase. These urban heat stress metrics were obtained from the human index module named HumanIndexMod in CLM5 (Buzan et al., 2015), defined by:

$$\begin{aligned}\mathrm{NWS\_HI} = & -42.379 + 2.04901523 \times T_f + 10.14333127 \times \mathrm{RH} - 0.22475541 \times T_f \times \mathrm{RH} \\ & - 6.83783 \times 10^{-3} \times T_f^2 - 5.481717 \times 10^{-2} \times \mathrm{RH}^2 \\ & + 1.22874 \times 10^{-3} \times T_f^2 \times \mathrm{RH} \\ & + 8.5282 \times 10^{-4} \times T_f \times \mathrm{RH}^2 - 1.99 \times 10^{-6} \times T_f^2 \times \mathrm{RH}^2,\end{aligned} \tag{3}$$

$$\mathrm{AT} = T_c + 3.3 \times \frac{V_p}{1000} - 0.7 \times U_{10} - 4, \tag{4}$$

$$\mathrm{sWBGT} = 0.567 \times T_c + 0.393 \times \frac{V_p}{100} + 3.94, \tag{5}$$

$$\mathrm{HUMIDEX} = T_c + \frac{5}{9}\left(\frac{V_p}{100} - 10\right), \tag{6}$$

and

$$\mathrm{DI} = 0.5 \times T_w + 0.5 \times T_c, \tag{7}$$

where T_f is the air temperature in Fahrenheit (°F), RH is the relative humidity (%), T_c is the air temperature (°C), V_p is the vapor pressure (Pa), U_{10} is the 10-m winds $\left(\mathrm{m\ s^{-1}}\right)$, T_w is the 2-m wet-bulb temperature (°C) calculated by using Stull (2011) method:

$$\begin{aligned}T_w = & \; T_c \times \arctan\left(0.151977 \times \sqrt{\mathrm{RH} + 8.313659}\right) + \arctan(T_c + \mathrm{RH}) - \arctan(\mathrm{RH} - 1.676331) \\ & + 0.00391838 \times \mathrm{RH}^{3/2} \times \arctan(0.023101 \times \mathrm{RH}) - 4.686035.\end{aligned} \tag{8}$$

2.5.2. The Urban Surface Energy Budget

We used regression analysis to identify the impacts of roof albedo modification on urban energy fluxes (Section 3.2), using the surface energy balance introduced in CLMU as:

$$\mathrm{FSA} - \mathrm{FIRA} = \mathrm{FSH} + \mathrm{FLH} + (\mathrm{FGR} - \mathrm{AC} + \mathrm{HEAT}) - \mathrm{WASTEHEAT} - \mathrm{HEAT}, \tag{9}$$

where FSA is the urban absorbed solar radiation $\left(\mathrm{W\ m^{-2}}\right)$, FIRA is the urban net longwave radiation, FSH is the urban sensible heat, FLH is the urban total latent heat, FGR is the urban heat flux into urban surfaces, WASTEHEAT is the sensible heat flux from heating and cooling sources of urban waste heat, AC is the sensible heat flux put into the street canyon due to heat removed from air conditioning, and HEAT is the urban heat flux. There is a minimum indoor temperature to kick in heating in every grid cell and CLMU calculates HEAT when the indoor temperature is below the minimum. Similarly, CLMU calculates AC when the indoor temperature exceeds the maximum, but in particular, CLMU assumes that only a few regions have the setpoint set for air conditioning to kick in and hold TBUILD at some reasonable temperature (X. C. Li et al., 2024). Accordingly, the anthropogenic heat flux (AHF) to the climate system is modeled as comprising urban heating flux and sensible heat from both urban heating and air-conditioning waste heat, while excluding other heat sources like urban traffic and human metabolism due to a lack of suitable global data:

$$\mathrm{AHF} = \mathrm{HEAT} + \mathrm{WASTEHEAT}. \tag{10}$$

To examine how absorbed solar radiation would change by albedo increases under the SSP3-7.0 scenario, we conducted the statistical regression using the fixed effects model. In all simulations, both urban surface albedo and FSDS (Figure D1) are transient under the SSP3-7.0 scenario, thereby considered as independent variables in the regression model. We introduce a dummy variable μ_g to fix entity (grid cell) specific effects. That is, grid cells sharing the same urban albedo might have different performances of reflecting or absorbing solar radiation, given their specific landunit structure, morphological characters, and thermal properties. Fixing entity effects aimed to omit underlying factors within certain urban areas. The regression model is expressed as:

$$\mathrm{FSA}_{t,g} = \beta_1 \times \mathrm{ALB\_}_{t,g} + \beta_2 \times \mathrm{FSDS}_{t,g} + \mu_g, \tag{11}$$

where $\mathrm{FSA}_{t,g}$ is the absorbed solar radiation of a certain grid g at a certain time of t, $\mathrm{FSDS}_{t,g}$ is the incoming shortwave radiation, and $\mathrm{ALB\_}_{t,g}$ is the prescribed urban surface albedo parameter input (i.e., ALB_ROOF_DIF, ALB_ROOF_DIR, ALB_IMPROAD_DIF, ALB_IMPROAD_DIR, ALB_WALL_DIF, and ALB_WALL_DIR). β_1 and β_2 are the coefficients of the independent variables $\mathrm{ALB\_}_{t,g}$ and $\mathrm{FSDS}_{t,g}$, respectively. For instance, β_1 represents the change in the $\mathrm{FSA}_{t,g}$ for a one-unit change in the $\mathrm{ALB\_}_{t,g}$ holding $\mathrm{FSDS}_{t,g}$ as a constant. After initializing the prescribed albedo, the model calculates the surface reflectivity involving physical processes at each time step. The actual urban surface albedo α is a prognostic variable, calculated as the ratio of reflected solar radiation by incoming solar radiation in urban areas:

$$\alpha = \frac{\mathrm{FSDS} - \mathrm{FSA}}{\mathrm{FSDS}}. \tag{12}$$

We distinguished between urban surface albedo and actual albedo, as the former refers to characteristic albedo values assigned to different urban surfaces such as roof, wall, impervious road, and pervious road. In contrast, the latter provides a direct measurement of urban reflective properties under specific conditions such as the angle of the sun, atmospheric forcing, and surface conditions.

2.5.3. Urban Heterogeneity and Implication for Design Strategies

To meet the need for fine design, we examined the albedo cooling effects within the context of urban heterogeneity (Section 3.3), encompassing urban density classes (i.e., TBD, HD, and MD) and surfaces (i.e., roof, impervious road, and wall). We analyzed the impacts of urban albedo modifications on these urban features, taking into account their distinct unique morphological, thermal, and radiative properties. These characteristics are localized in grid cells, which leads to spatial variations across global urban areas. Besides focusing on urban temperature reduction, we assessed the implications of albedo modifications for developing urban climate-sensitive design strategies (Section 4). We raised particular concerns about the indoor thermal environment, with a focus on balancing energy consumption and savings by latitude.

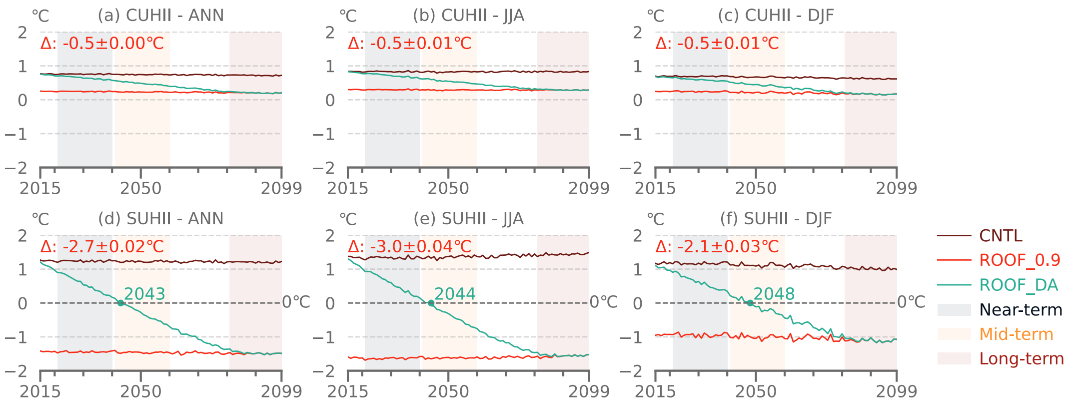

Figure 3. Global-mean canopy urban heat island intensity (CUHII) and surface urban heat island intensity (SUHII) during 2015–2099 in the CNTL, ROOF_0.9, and ROOF_DA simulations. Δ denotes the reductions of global-mean±std urban temperature by ROOF_0.9 minus CNTL. (a), (d) ANN denotes the annual mean. (b), (e) JJA denotes the summer (June–July–August) mean. (c), (f) DJF denotes the winter (December–January–February) mean. Dots in (d)–(f) denote the years when the ground temperatures in urban and rural areas are the same.

3. Result and Discussion

3.1. Continuous Mitigation of Urban Heat With Transient Roof Albedo

We first assessed the impacts of urban roof adaptation strategies on urban thermal environments through the CNTL, ROOF_0.9, and ROOF_DA simulations. In the CNTL simulation, without urban climate intervention, the annual-mean CUHII and SUHII during 2015–2099 is 0.7 ± 0.02°C (mean ± std) (Figure 3a) and 1.2 ± 0.03°C (Figure 3d), respectively. Seasonal patterns reveal that the mean CUHII is higher by 0.2 ± 0.03°C in the boreal summer (JJA) than in the boreal winter (DJF). Higher CUHII in summer than in winter is consistent with some case studies (e.g., Schatz & Kucharik, 2014; Yao et al., 2021; Ünal et al., 2020) but not all (e.g., P. Yang et al., 2013). While CUHII does not show large fluctuations over time, global warming accelerates SUHII, particularly in summer, where SUHII rises from 1.4°C in 2015 to 1.5°C in 2099 (Figure 3e). The warmer thermal environment in urban areas leads to less snow so that actual surface albedo in winter decreases by 0.003 from 2015 to 2099 (Figure C1b).

In the ROOF_0.9 simulation, we replaced the default roof albedo values (as set in the CNTL simulation) with 0.9 across all urban areas over the globe for the entirety of the simulation period. This modification leads to a large decrease in the annual-mean CUHII from 0.7°C to 0.2°C (−0.5 ± 0.005°C), and in the annual-mean SUHII from 1.2°C to −1.5°C (−2.7 ± 0.02°C), indicating a more pronounced response of SUHII to changes in roof surface albedo. This is because the surface temperature is more sensitive to the surface energy budget than the air temperature (Bateni & Entekhabi, 2012; Smith et al., 2023). Changes in surface albedo directly modify the surface energy budget and thus directly affect surface temperature. While higher albedo reflects more solar radiation, the reflected radiation does not directly heat the air in the urban canyons. Instead, high albedo primarily cools urban surfaces, which then results in less heat being transferred to the air through the emission of longwave radiation and other heat transfer processes. Thus, the interactions between the land surface and the canopy air within the thin surface layer modulate temperature perturbations (P. Hou et al., 2013), causing air temperature changes to respond less prominently to changes in surface albedo. In addition, the difference in SUHII reduction between summer and winter is also larger than in CUHII reduction. Specifically, the reduction in JJA-mean SUHII reaches −3.0 ± 0.04°C (Figure 3e), greater than the DJF-mean SUHII reduction of −2.1 ± 0.03°C (Figure 3f). This more substantial reduction in SUHII during summer is primarily because of the higher solar radiation. In summer, the increased solar intensity means that any enhancement in albedo results in a greater decrease in absorbed heat and surface temperatures. In winter, snow cover typically increases the surface reflectivity, but this additional reflective effect is relatively small compared to summer. Moreover, the insulating properties of snow can retain heat (Malevich & Klink, 2011), making the reduction in SUHII less pronounced.

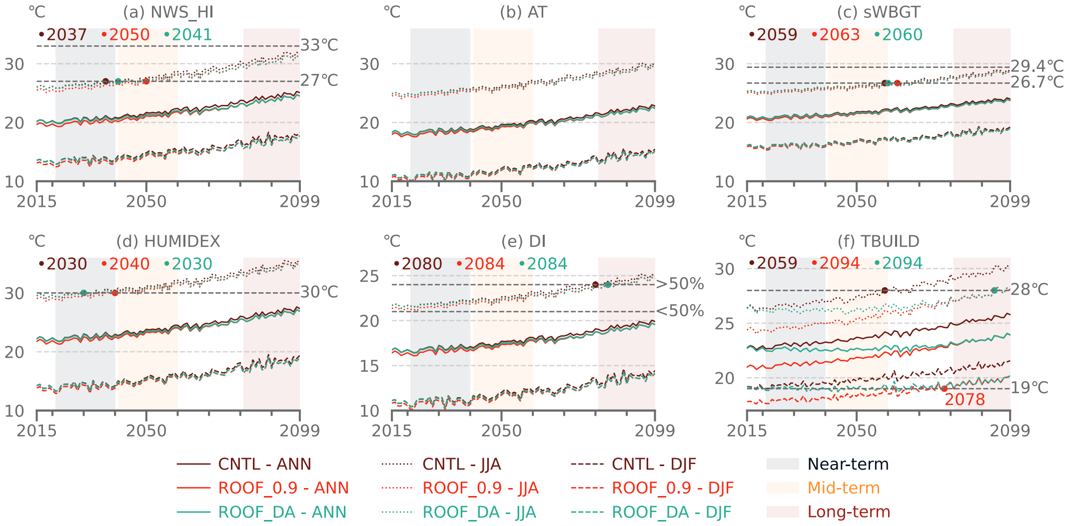

Figure 4. Global-mean urban heat stress indices and indoor temperature during 2015–2099 in the CNTL, ROOF_0.9, and ROOF_DA simulations. Referring to Buzan et al. (2015), (a) 2-m U.S. National Weather Service Heat Index (NWS_HI) at 27°C marks the threshold of caution, while at 33°C, it signifies extreme caution. (b) 2-m apparent temperature (AT) lacks a specific description of thresholds. (c) 2-m simplified wet-bulb globe temperature (sWBGT) between 26.7°C and 29.3°C indicates alert and between 29.4°C and 31.0°C indicates caution. (d) 2-m humidity index (HUMIDEX) at 30°C is the critical threshold of some discomfort. (e) 2-m discomfort index (DI), where 21–24°C indicates less than half of the population experiencing discomfort and above 24°C denotes over half of the population in discomfort. (f) Indoor air temperature (TBUILD) is recommended to be within the range of 19–28°C for general activities (Enescu & Flanner, 2017). Dots in (a), (d), (e), and (f) denote the years when reaching critical thresholds.

Comparing the CNTL and ROOF_0.9 simulation results, an annual-mean reduction in CUHII by 0.5°C aligns with the findings by Oleson et al. (2010a), which reports a decrease in annual-mean CUHII by 0.4°C (from 1.2°C to 0.8°C), as a result of increasing roof albedo from 0.32 to 0.9. The differences in annual-mean CUHII values between our study and the findings of Oleson et al. (2010a) can be partly attributed to variations in simulation set-ups. Their study spanned from 1941 to 1999, relying on present-day atmospheric forcings, whereas our projections extended from 2015 to 2099 under the SSP3-7.0 scenario. Additionally, our land-only simulations, conducted with the CLM5 coupled with an updated building energy model, differ from Oleson et al. (2010a)'s atmosphere–land coupled simulations that used CLM3.5 with a coarser grid spacing of 1.9° latitude by 2.5° longitude.

In the ROOF_DA simulation, we observed an instant response of urban thermal environments to transient albedo changes, evidenced by a continuous decrease in CUHII and SUHII intensity. The reduction rate of CUHII (ΔCUHII per 0.01 increase in roof albedo) is quantified as -0.009 ± 0.0001°C, as shown in Figure 3a, and ΔSUHII at -0.04 ± 0.0002°C, as shown in Figure 3d. With increasing roof albedo by 0.01 per year, annual-mean SUHII becomes negative beginning in 2043. Negative SUHII means that urban surface temperatures with high albedo could be even lower than those in rural areas. This suggests the potential of adaptive albedo modifications in mitigating urban heat island effects. Increasing albedo also narrows the difference in SUHII between summer and winter, where SUHII in summer would be lower than in winter since 2030 (Figure B1b). In contrast, CUHII would remain positive values and generally higher than in winter. This also indicates that despite cooler surfaces, buildings continue to emit and retain heat and the overall urban areas still experience daily higher temperatures within the canopy layer than rural areas. The continuous downward trends reflect the transient representation of albedo variables in CLMU, where the "UrbanAlbedoMod" module computes transient urban albedo parameters in a given year, incorporating new albedo values into each simulation time step. The annual-mean CUHII started at 0.8°C in 2015, similar to the counterpart in the CNTL simulation, and would diminish to 0.2°C by 2099, aligning with the counterpart in the ROOF_0.9 simulation. The final results in ROOF_0.9 and ROOF_DA simulations are almost the same, indicating that in offline simulations, the modeled urban environment is largely constrained by atmospheric forcing while variations of initial condition in the land model play a minimal role.

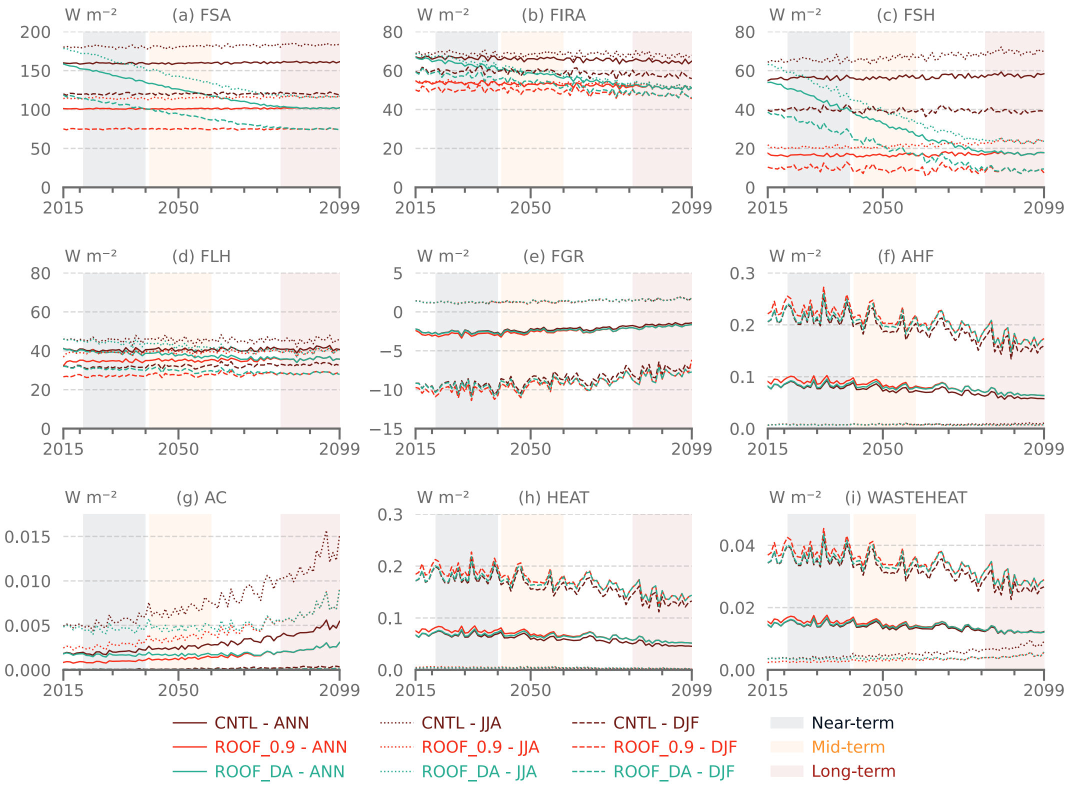

Figure 5. Annual-mean grid-level urban energy changes. (a) Urban absorbed solar radiation (FSA). (b) Urban net longwave radiation (FIRA). (c) Urban sensible heat (FSH). (d) Urban total latent heat (FLH). (e) Heat flux into urban surfaces (FGR). (f) Anthropogenic heat flux that goes into the climate system (AHF). (g) Urban air-conditioning flux (AC). (h) Urban heating flux (HEAT). (i) Sensible heat flux from heating and air-conditioning sources (WASTEHEAT).

In parallel with CUHII and SUHII, transient albedo also impacts the temporal pattern of urban heat stress indices, as seen in Figures 4a–4e. These indices follow the rising trend of atmospheric forcing over the study period (Figure D1) and show varying timing of crossing their critical thresholds. The comparison between ROOF_0.9 and CNTL reveals annual-mean reductions in heat stress indices: NWS_HI by 0.6 ± 0.007°C, AT by 0.4 ± 0.003°C, sWBGT by 0.3 ± 0.002°C, HUMIDEX by 0.5 ± 0.004°C, and DI by 0.3 ± 0.003°C. These findings indicate that a higher albedo mitigates the rate at which these indices reach critical thresholds. For instance, NWS_HI in the CNTL simulations hit its critical threshold (27°C) in 2037 JJA, nearing the end of the near-term period. In contrast, in the ROOF_0.9 simulation, NWS_HI does not reach its critical threshold until the summer of 2050, delaying the occurrence by thirteen years compared to the CNTL simulation (Figure 4a). Meanwhile, the CNTL and ROOF_DA simulation shows HUMIDEX exceeding its critical discomfort threshold of 30°C by 2030 JJA, 10 years before the ROOF_0.9 simulation, depicted in Figure 4d. Regarding the DI, more than half of the population experiences heat discomfort from 2080 onwards in the CNTL simulation. Implementing a 0.9 roof albedo in both ROOF_0.9 and ROOF_DA simulations delays reaching this upper discomfort threshold by 4 years, as shown in Figure 4e. This extension in the time before reaching hazardous heat levels is particularly noteworthy as it allows for extended planning and implementation of additional heat mitigation strategies, potentially reducing heat-related health risks and energy demands over a longer period. Although regional variations in thermal comfort thresholds exist, we use universal thresholds to ensure consistency with previous studies (Buzan et al., 2015; Oleson et al., 2015).

Furthermore, indoor air temperature (TBUILD) is influenced by both the background climate changes and modifications to urban roof albedo, as depicted in Figure 4f. Within the CNTL simulation, the JJA-mean TBUILD crosses the critical threshold of 28°C in 2059, escalating to 30.1°C by 2099, marking an increase of 3.7°C over 85 years. To sustain a comfortable indoor environment, there will be a rising need for air conditioning in the future. Adjusting the roof albedo to 0.9 moderates indoor temperatures, resulting in an annual-mean TBUILD reduction of 1.8±0.02°C when comparing ROOF_0.9 with CNTL. In the ROOF_DA simulation, the gradual increase in roof albedo effectively delays crossing the upper critical threshold of thermal comfort until 2094, showcasing its long-term benefits. However, a high roof albedo also entails drawbacks for the winter indoor thermal environment. In the CNTL simulation, the mean TBUILD during boreal winter (DJF) remains above the lower comfort threshold of 19°C starting from 2015, suggesting a comfortable indoor temperature in DJF. Conversely, in ROOF_0.9 simulations, DJF-mean TBUILD falls below 19°C from 2015 to 2078, necessitating additional heating (Figure 5h) to maintain thermal comfort in winter.

3.2. The Urban Surface Energy Budget Responses to Roof Albedo Modifications

Analysis of the urban energy budget, using CNTL, ROOF_0.9, and ROOF_DA simulations, reveals that urban radiation and turbulent fluxes exhibit consistent patterns alongside atmospheric forcing, without large deviation over 85 years (Figures 5a–5d). The CNTL simulation sees urban absorbed solar radiation (FSA) experiencing an annual increase of 0.94%, from 159.88W m^{-2} in 2015 to 161.38W m^{-2} in 2099. The FSA rise of 1.50W m^{-2} is attributed to the FSDS with a similar increase of 1.60W m^{-2} from 2015 to 2099. Building energy consumption adapts to increasing TBUILD due to more absorbed heat, influencing heat transfer to the ground and climate system (Figures 5e–5i). Specifically, air conditioning flux (AC) increases from 0.005W m^{-2} in the summer of 2015 to 0.015W m^{-2} by the summer of 2099, whereas urban heating demand declines from 0.17W m^{-2} in the winter of 2015 to 0.13W m^{-2} by the winter of 2099. As a result, the anthropogenic heat flux (AHF) entering the climate system sees a 28.8% reduction, from 0.081W m^{-2} to 0.058W m^{-2}, lying below the estimate of 0.19W m^{-2} by Flanner (2009) and the 0.15W m^{-2} by Jin et al. (2019). This discrepancy is likely due to CLMU's building energy model calculating AHF in response to indoor temperature feedback, in contrast to assessments based on broader energy consumption metrics.

The ROOF_DA simulation illustrates the transient response of radiation and heat flux to increasing roof albedo. The annual-mean FSA reduction rate is 0.94 ± 0.0006W m^{-2} (Table C1), with albedo modifications manifesting more distinctly seasonally; the JJA-mean FSA reduction is 1.06 ± 0.0008W m^{-2}, while the DJF-mean sees a slightly different rate (0.73 ± 0.0008W m^{-2}). This seasonal variability of solar radiation absorption mainly results from atmospheric forcing, where incoming solar radiation varies over seasons. Increasing the roof albedo means more solar radiation is reflected rather than absorbed by the roof. With less absorbed solar radiation, the roof surface is cooler, resulting in a decrease in net longwave radiation emission (FIRA) as cooler surfaces emit less longwave radiation. Given that the sensible heat flux (FSH) is computed from the difference between atmospheric forcing temperature and canyon air temperature, the subsequent decrease in canyon air temperature leads to less FSH. Cooler surfaces also have lower rates of evaporation since evaporation is a temperature-dependent process, resulting in decreasing latent heat flux (FLH). Generally, the reduction of annual-mean FSH is larger than the reduction of annual-mean FLH, suggesting cooling effects on the urban surface (Schlaerth et al., 2023). Adopting high albedo reduces associated urban radiation and heat flux except for AHF. By increasing roof albedo by 0.01 per year, AC moderately fluctuates around 0.005W m^{-2} before the 2070s, mitigating the warming effects where AC continuously increases in the CNTL simulation. At the same time, the cooling effects of higher albedo in winter require more heating, where urban heating flux (HEAT) in the ROOF_DA is almost the same as the counterpart in the ROOF_0.9 simulation since the 2060s. Additionally, the introduction of a 0.9 urban roof albedo in the ROOF_0.9 simulation markedly lowers the annual-mean FSA from 159.90 ± 0.96W m^{-2} to 101.24 ± 0.60W m^{-2}, yielding an upper limit of around 60Wm^{-2} FSA reduction by the end of the century.

3.3. Urban Landunit and Surface Heterogeneity With Urban Albedo Modifications

Exploring urban albedo adaptations across urban roofs, impervious roads, and walls underscores the varied impacts on urban heat island intensity, urban heat stress, and indoor temperature, with roof albedo modifications showing the most substantial influence. The annual-mean CUHII decrease rates in ROOF_DA, IMPROAD_DA, WALL_DA simulations are −0.009 ± 0.0001°C, −0.001 ± 0.0005°C, and −0.004 ± 0.0008°C, respectively, as shown in Figure 6a. For SUHII, the decrease rates are −0.04 ± 0.0002, −0.003 ± 0.0001, −0.009 ± 0.0002°C, respectively (Figure 6d). Except for modifying roof albedo, using high impervious road or roof albedo cannot fully counteract urban heat island effects, where SUHII and CUHII remain positive values by the end of the century. The marginal urban temperature reductions with increased albedo in walls or impervious roads are linked

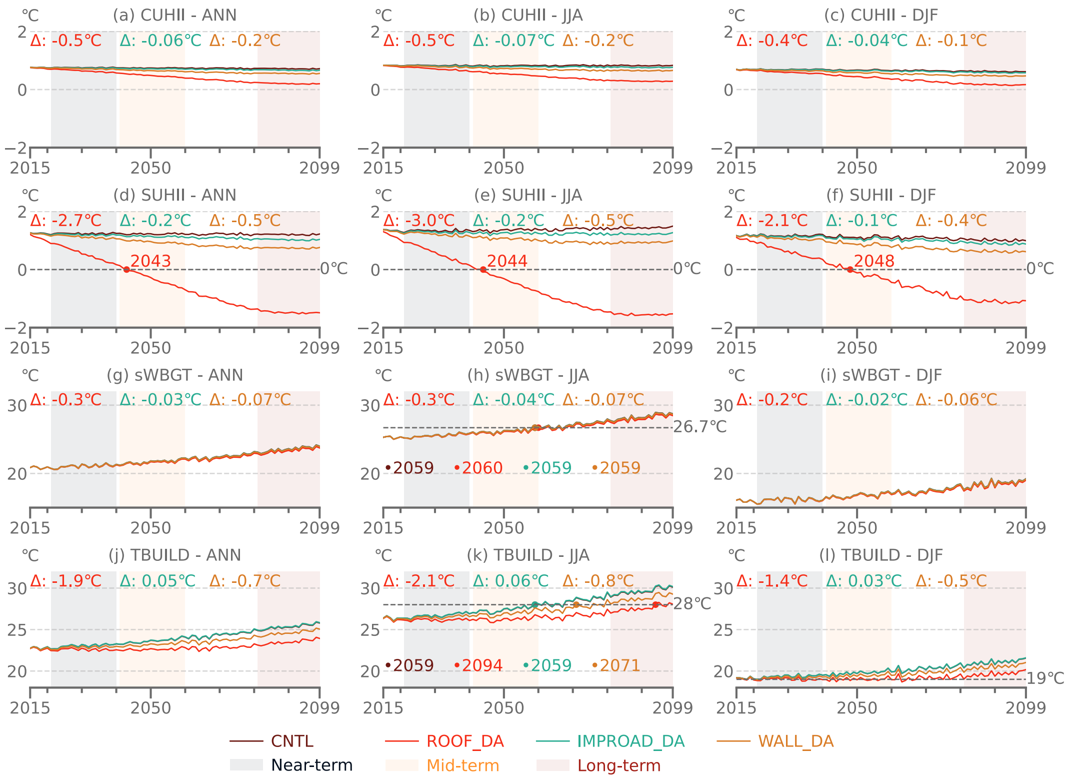

Figure 6. Comparisons of global-mean CUHII, SUHII, SWGBT, and TBUILD induced by urban surface albedo changes during 2015–2099. Δ denotes mean ROOF_DA minus CNTL, IMPROAD_DA minus CNTL, and WALL_DA minus CNTL in 2099. (a), (d), (g), (j) ANN denotes the annual mean. (b), (e), (h), (k) JJA denotes the summer mean values during the June–July–August periods. (c), (f), (i), (l) DJF denotes the winter mean values during the December-January-February periods. Dots in (d)–(f) denotes the years when the ground temperatures in urban and rural areas are the same. Dots in (h) denote the years when the sWBGT crosses the critical threshold of alert (26.7°C). Dots in (k) denote the years when JJA-mean TBUILD reaches the upper threshold of thermal comfort at 28°C.

to the marginal decrease in FSA, depicted in Figure C4a. TBUILD decreases across albedo increases, except in the IMPROAD_DA simulation, where a 0.9 impervious road albedo results in a slight annual-mean TBUILD increase of 0.1°C by 2099 (Figure 6j). This rise in indoor temperature, related to the reflectivity of roads, has been reported by Salvati et al. (2022), attributing to the incident diffuse radiation trapped within the urban street canyon. The annual-mean urban actual surface albedo α in ROOF_DA simulation is 0.0046 (Figure C1a), which is close to the expected value of 0.0044, calculated as a 0.01 increase in described albedo multiplied by the percent of roof area in the urban horizontal surface (0.44). This indicates that changes in the prescribed roof albedo are fully reflected in the actual roof albedo. In contrast, the annual-mean α in IMPROAD_DA simulation is 0.0005, which is lower than the expected value of 0.0015, calculated as a 0.01 increase in described albedo multiplied by the percent of impervious road area in urban horizontal surface (0.15). Compared to roofs, which directly reflect solar radiation to the atmosphere (Figure C2a), solar radiation reflected by walls or impervious roads bounces between buildings (Figures C2b and C2c), increasing overall heat retention within the canyon. This repeated reflection within the canyon further increases the absorption by walls and roads, reducing the efficiency of surface reflectivity in mitigating solar radiation.

Comparing urban thermal environments across TBD, HD, and MD areas shows daytime CUHII is more substantially reduced in TBD than in HD and MD (Figures 7a–7c). In the CNTL simulation, daytime CUHII averages at 2.0 ± 0.03°C in TBD, compared to 0.7 ± 0.02°C in HD and 0.5 ± 0.02°C in MD. The ROOF_DA simulation induces daytime CUHII reductions of 0.03 ± 0.0002°C in TBD, 0.02 ± 0.0002°C in HD, and 0.01 ± 0.0001°C in MD. Morphological (i.e., canyon height-to-width ratio, roof fraction, and wall and building thickness), surface thermal (i.e., volumetric heat capacity, thermal conductivity), and radiative (i.e., emissivity) properties (Oleson

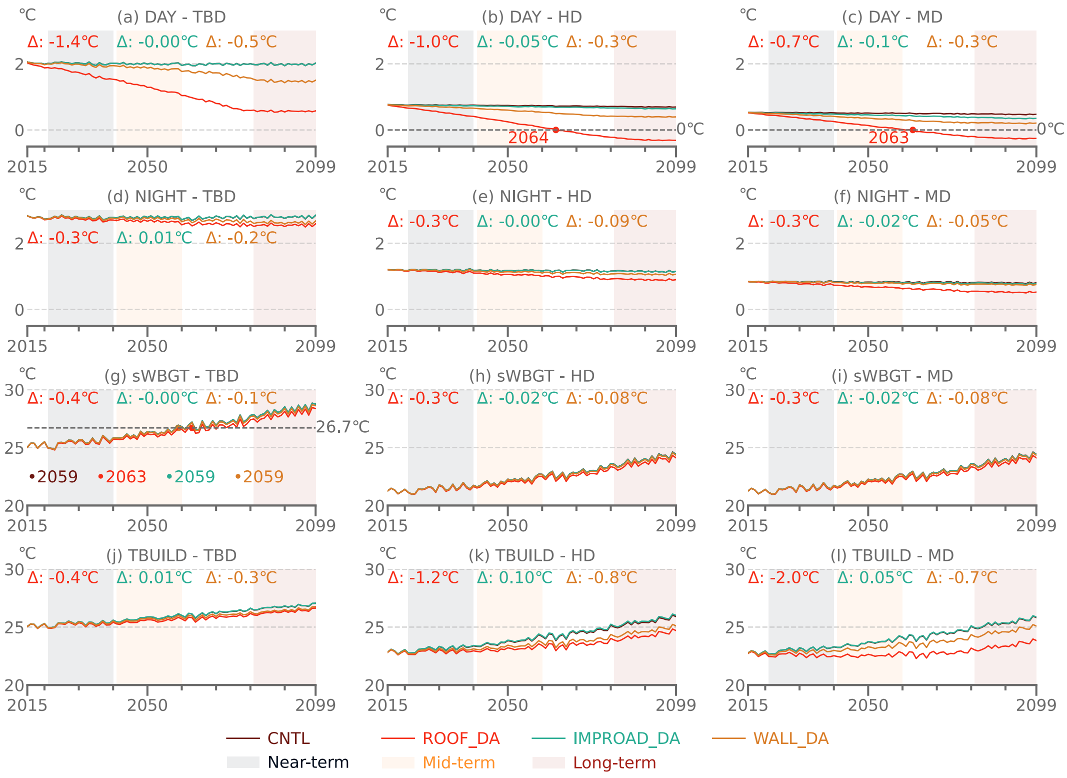

Figure 7. Urban landunit heterogeneity during 2015–2099. (a)–(c) DAY denotes the daytime canopy urban heat island intensity (CUHII) by contrasting annual-mean urban and rural daily maximum of average 2-m air temperature. (d)–(f) NIGHT denotes the night CUHII by contrasting the annual-mean urban and rural daily minimum of average 2-m air temperature. (g)–(i) Annual-mean 2-m simplified wet-bulb globe temperature (sWBGT). (j)–(l) Annual-mean indoor temperature (TBUILD). Δ in red, green, and yellow denote the annual-mean ROOF_DA minus CNTL, IMPROAD_DA minus CNTL, and WALL_DA minus CNTL in 2099, respectively. Dots in (b)–(c) denote the years when the daytime 2-m air temperatures in urban and rural areas are the same. Dots in (g) denote the years when sWBGT crosses the critical threshold of alert (26.7°C).

et al., 2008) over urban landunits contribute to differences in the responses of the thermal environment to albedo changes. As TBD is characterized by a narrow and deep canyon, and a large percentage of roofs and impervious roads (Figure C3a), it faces the most severe heat stress risk. sWBGT in TBD would cross the critical threshold of 26.7°C in 2059 (Figure 7g) while sWBGT in HD and MD remain below the critical threshold. Increasing roof albedo in TBD could achieve the most efficient cooling effects, where daytime CUHII decreases most (−1.4°C). The deep urban canyons in TBD with large height-to-width ratios contribute to heat retention, where daytime CUHII remains positive over the years despite applying high urban albedo. In contrast, thermal conditions in HD and MD are not as severe as in TBD, where annual-mean daytime CUHII in HD and MD drops below 0°C around the 2060s (Figures C3b and C3c). Despite little solar radiation at night, we also observed nighttime CUHII reductions in ROOF_DA (0.3°C) and WALL_DA (0.1–0.2°C) simulations. By reducing the heat absorbed during the day, less heat is stored within the canyon, and consequently, less heat is released at night. This leads to a modest reduction in nighttime urban temperature and CUHII. Increasing roof or wall albedo results in a consistent pattern: the largest reduction in daytime CUHII occurs in TBD, followed by HD and MD areas. But when impervious road albedo is increased, the pattern differs. In IMPROAD_DA simulation, the reduction of daytime CUHII in MD reaches 0.12°C by 2099, higher than in the counterpart in TBD (0°C) and in HD (0.05°C). MD has a wide and low canyon, which makes it easier for solar radiation to reach the canyon floor directly, then be reflected and escape from the canyon (Figure C3c). Additionally, impervious roads with high reflectivity do not markedly reduce nighttime CUHII and sWBGT, and even slightly increase the annual-mean indoor temperature in HD by 0.1°C (Figure 7k).

Moreover, compared to single-surface albedo modification, compounding albedo modification can achieve synergistic cooling effects (Figure C4). Synergistic reflection is a feedback loop, for example, solar radiation reflected off a high-albedo road surface might then strike a high-albedo wall or roof, reflecting again rather than being absorbed. In the ROOF_IMPROAD_DA simulation, a 0.01 albedo increment in both roofs and impervious roads reduces the annual-mean FSA by 1.06W m^{-2} (Table C1), slightly higher than the sum of FSA reduction in ROOF_DA (0.94W m^{-2} per 0.01 roof albedo increase) and IMPROAD_DA (0.11W m^{-2} per 0.01 impervious road albedo increase) simulations. The modeled FSA reduction in ROOF_IMPROAD_DA simulation is lower than the value (1.27W m^{-2}) calculated by Akbari et al. (2009). This discrepancy may result from the differences in the FSDS between the two studies, with our simulations showing an FSDS of 193.6 ± 1.1W m^{-2} compared to the 206W m^{-2} assumed by Akbari et al. (2009). The allocation of urban horizontal surfaces in CLMU, with roofs and impervious roads constituting 44.3% and 15.5%, diverges from Akbari et al. (2009)'s assumption of 25% for roofs and 35% for impervious roads, influencing the effects on FSA. Additionally, our simulations show different actual reflectivity between roofs and impervious roads while previous studies used to assume both horizontal surfaces with similar reflectivity. ROOF_IMPROAD_WALL_DA simulation shows compounded effects on urban heat variations, where FSA reduction (1.40W m^{-2}) is 0.10W m^{-2} more than the sum of FSA reduction from three single-surface albedo modifications. When albedo is increased on multiple surfaces, the overall reflectivity of the urban environment increases.

4. Implications for Urban Climate-Sensitive Design Strategies

Our experimental simulations extend beyond previous studies on quantifying the effects of white roofs and cool pavements through global urban climate modeling (Table 1), offering insights into albedo-induced adaptation effects in terms of urban heterogeneity, global spatial variations, and seasonal differences. The distinct impacts of modifying albedo on roofs, impervious roads, and walls characterize their potential in future urban design and planning. For instance, a 0.01 increment in roof albedo leads to a 0.94 ± 0.0006W m^{-2} decrease in FSA, whereas the same increase in impervious road and wall albedo decreases FSA by 0.11 ± 0.0001W m^{-2} and 0.24 ± 0.0002W m^{-2}, respectively. Increasing roof albedo effectively reflects solar radiation, reducing the heat absorbed and stored in the urban fabric. The differential impacts highlight the important role of roof albedo modification in lowering urban temperature globally, as opposed to the relatively modest contributions from impervious road and wall albedo modifications. Moreover, special attention should be paid to TBD areas, where thermal conditions pose greater challenges compared to MD and HD areas. Despite the application of high roof albedo, TBD areas are more prone to reaching the sWGBT's critical threshold of alert at 29.3°C (Figure 7g). These findings underscore the importance of targeted interventions in densely built-up areas.

Multiple metrics of urban heat stress indices with varying timing of crossing their critical thresholds reflect the complexity and multifaceted nature of heat stress. For instance, implementing a continuous increase in roof albedo delays the timing of NHW_HI and DI crossing their critical thresholds by 4 years, while it minimally influences the timing of sWBGT and HUMIDEX crossing their critical thresholds (Figure 4). Additionally, HUMIDEX reports higher numerical values of urban heat stress compared to other indices, leading to an earlier crossing of the critical threshold of some discomfort at 30°C. By understanding that different indices respond differently to high albedo, urban planners can tailor their approaches to address immediate, mid-term, and long-term heat stress risks. Considering the near-term projection that JJA-mean NWS_HI and HUMIDEX will surpass their critical thresholds around 2030 to 2040, the near-future period, this timeline suggests a critical window for implementing immediate actions.

Spatial analysis of urban temperature reductions reveals pronounced disparities, with lower annual-mean reductions in Southeast Asia, and Southern China (Figure 8a). The JJA-mean reduction in urban surface temperature is 1.2 ± 0.5°C (Figure 8b), where reductions in northern mid-high latitude areas, such as Europe, are greater than in low-latitude areas, such as India and South Asia. This pattern is reversed when entering winter (Figure 8c), highlighting seasonal and spatial differences. Elevated impervious road albedo is observed to cool certain areas such as Eastern China (Figures 8d–8f), whereas central Europe and Southeast Asia see advantages from increased wall albedo (Figures 8g–8i).

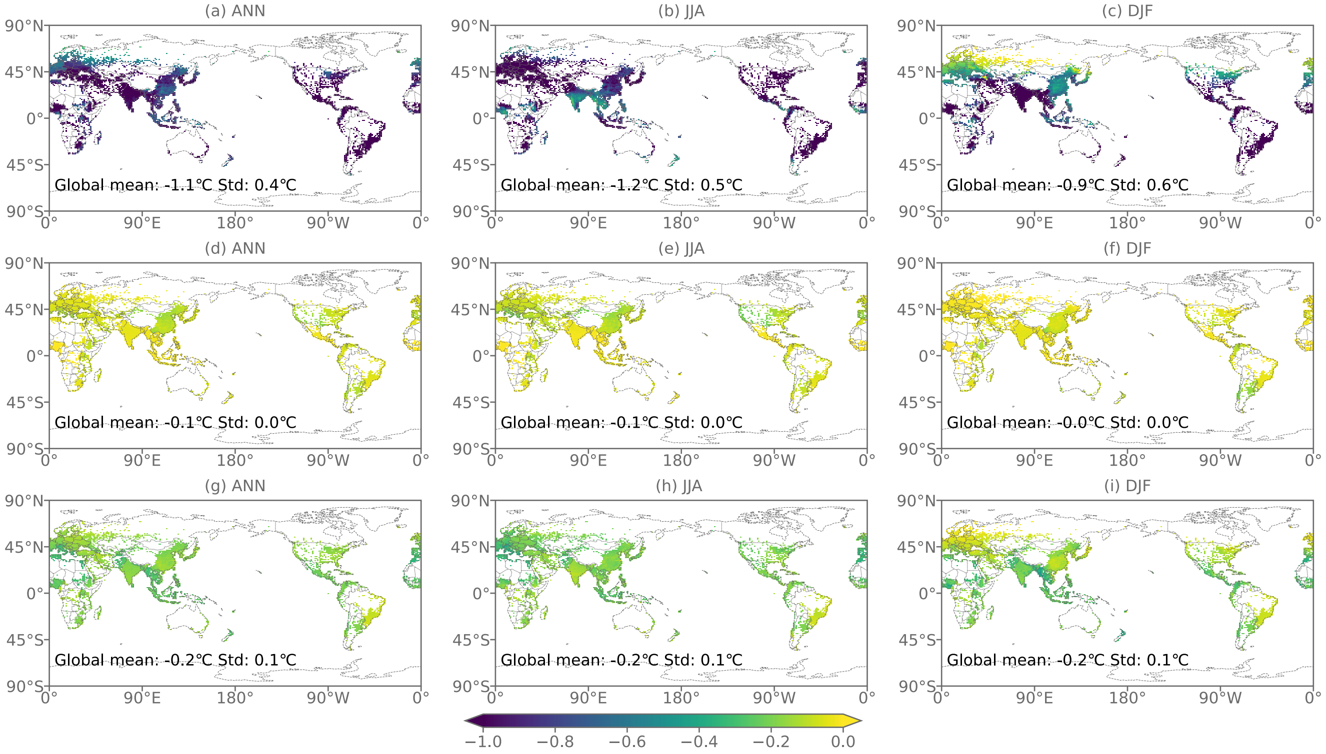

Figure 8. Reductions of urban surface temperature (ΔTG_U) in 2040 (the end of near-term). (a)–(c) ROOF_DA minus CNTL. (d)–(f) IMPROAD_DA minus CNTL. (g)–(i) WALL_DA minus CNTL.

The indoor thermal environment emerges as another factor in formulating adaptation strategies involving urban albedo modifications. By 2040, the JJA-mean reduction in indoor temperature resulting from the ROOF_DA compared to CNTL simulations is approximately 0.7 ± 0.2°C, similar to the DJF-mean reduction 0.7 ± 0.5°C. When resolved by latitude, urban areas at 42.88°N latitude experience the maximum decrease of JJA-mean TBUILD (1.2°C) and urban areas at 49.48°S face the maximum DJF-mean TBUILD decrease (2.0°C) (Figures 9a–9c). However, the indoor cooling effects stemming from urban albedo modifications are not globally consistent, particularly in high-latitude regions that face increased demands for heating. In 2040, the annual-mean AC reduces to 0.0009W m^{-2}, a decrease of 0.0003W m^{-2} from the CNTL simulation. Conversely, the annual-mean HEAT increases by 0.002W m^{-2}, nearly 10 times more than the AC reductions. We need to acknowledge that our quantification of HEAT and AC is dependent on the minimum and maximum indoor temperature, which remains uncertain for parameterizing the global building energy use. The AC reduction could be used for quantifying energy-saving when more realistically considering air conditioning adoption in the future (X. C. Li et al., 2024). The trade-off between cooling efficiency in summer and energy consumption in winter should be particularly considered in the high-latitude regions. Viewed from a long-term perspective, the annual total demands for air conditioning and heating in simulations incorporating transient albedo modifications show an upward trend in the urban areas located beyond 30°N and 25°S latitudes (Figure 10).

To overcome the constraints associated with static cooling roofs, current innovations are exploring thermotropic materials capable of changing colors from dark to light in response to temperature variations throughout the day or across seasons (Sharma et al., 2017; Ye et al., 2012). The potential for advancing the evaluation of transient material characteristics, employing monthly or even more frequent calculations, is promising within the framework of the transient urban albedo scheme. Architecture designs incorporating cooling envelopes and adaptive materials should proceed with caution, recognizing that high albedo strategies may not be universally applicable. Assessing such strategies should extend beyond the immediate impacts on urban temperature and building energy demands. Additionally, increasing urban surface albedo is a passive design strategy (Oliveira et al., 2009) that relies on the inherent properties of materials rather than mechanical systems to achieve cooling.

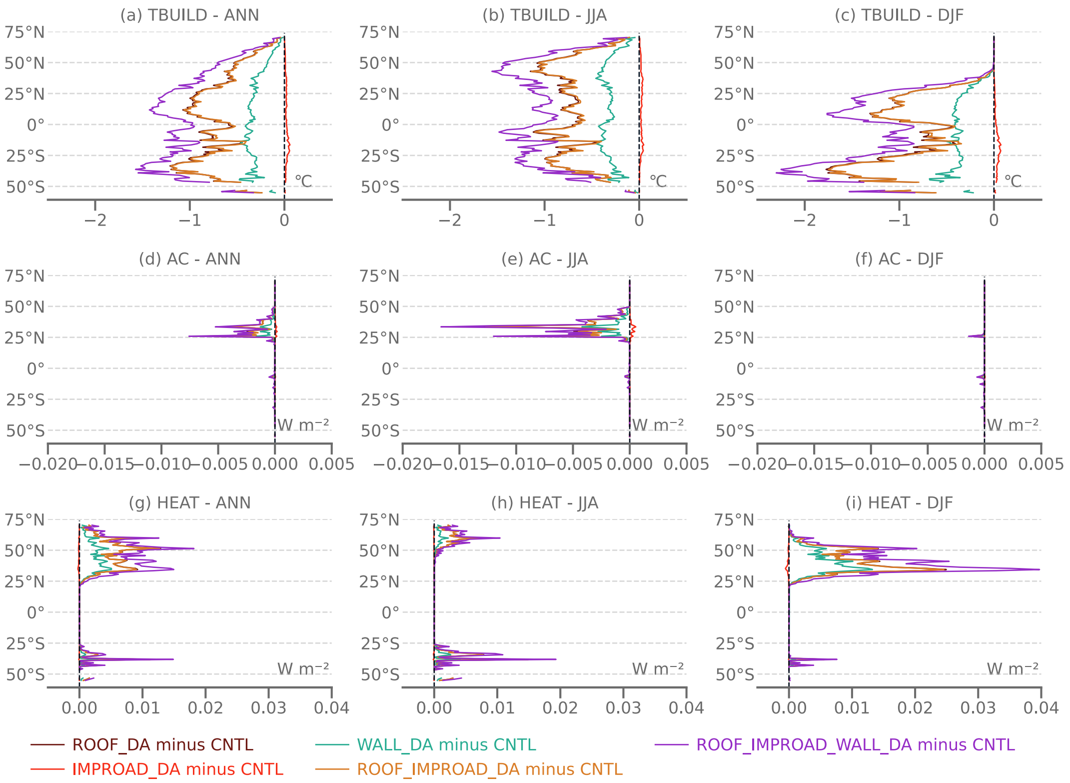

Figure 9. Latitude variations of indoor temperature (TBUILD), air conditioning (AC), and heating (HEAT) in 2040 (the end of near-term).

Its impact on global climate is statistically insignificant (Zhang et al., 2016) as it could only reduce energy use but could not generate energy or might not have a net positive impact on climate change as active design strategies such as green roofs and solar panels. As achieving cooling by increasing albedo alone is limited in its magnitude, we should consider other urban climate adaptation strategies meanwhile.

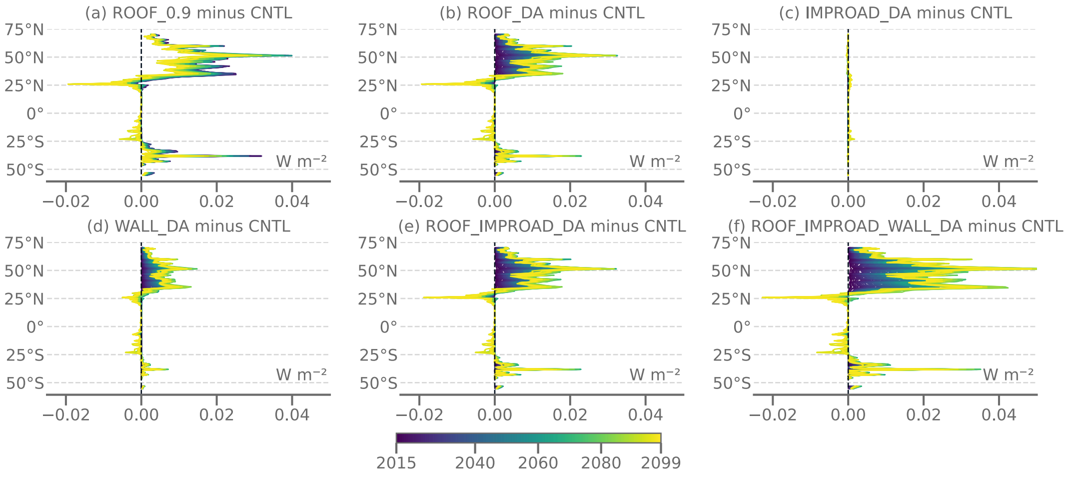

Figure 10. Annual-mean air conditioning (AC) plus heating (HEAT) from 2015 to 2099.

5. Conclusions

In this study, we developed a new transient urban surface albedo scheme within the Community Earth System Model (CESM) to explore the dynamic nature of urban climate adaptation strategies across urban surfaces including roofs, impervious roads, and walls. This new scheme allows for the evaluation of urban surface albedo modification impacts globally, focusing on urban thermal environments (e.g., urban heat island, urban heat stress, and indoor temperature), the urban energy budget, and the complexity of urban heterogeneity. Our findings underscore that the urban thermal environment, especially the urban absorbed solar radiation, responds to transient urban albedos over time, with roof albedo modifications being notably effective, followed by wall and impervious road albedo modifications. Implementing an annual increase of 0.01 in roof albedo is expected to reduce the annual-mean canopy urban heat island intensity from 0.8°C in 2015 to 0.2°C by 2099. Comparisons across ROOF_DA, IMPROAD_DA, and WALL_DA simulations shed light on the role of urban surface heterogeneity in influencing the local urban climate. Furthermore, our findings indicate that higher albedo configurations are especially effective in cooling environments within tall building districts, compared to high and middle-density areas.

The simulations underscore the pressing need for urban heat mitigation, highlighted by the projection that indices such as June–July–August mean National Weather Service Heat Index and 2-m humidity index will surpass critical thresholds by the end of the near-term (2021–2040). Despite practical considerations indicating that urban albedo might not achieve ideal levels as the simulations, this study aims to provide guidance for urban climate-sensitive design and policy development through modifications to urban albedo on a global scale across various time frames. It emphasizes the importance of holistic strategy selection over singular solutions like white roofing, urging consideration of localized factors such as geographical location, urban density types, and surface properties that affect urban albedo's impact on urban thermal environments, energy usage, and overall urban climate.

Acknowledging practical constraints, it is unlikely that urban albedo will reach the ideal value but rather remain at a relatively lower level. This study endeavors to inform the urban climate-sensitive design and adaptive policy-making by assessing the global impacts of changes in urban surfaces. Further examination of these impacts on specific cities should be achieved by employing simulations at higher resolutions. Earth system models are moving forward to kilometer-scale resolutions (Haarsma et al., 2016; L. Li et al., 2024; Schär et al., 2021), offering the potential to resolve urban fractions more realistically. This might make a difference in urban climate modeling under the Earth system model framework, particularly in simulating urban climate with greater impacts on the interactions between the atmosphere and urban surfaces. One of the limitations of the present study is that we used land-only simulations, where one-way atmospheric forcing constrains the feedback from the static urban surfaces. Consequently, we did not examine the impacts of transient albedo on global warming patterns. Although the interaction between urbanization and climate change is largely one-way at the global scale due to the currently small urban footprint, on regional scales where urban land changes are prominent, evidence shows two-way interactions (Chakraborty & Qian, 2024). This will be especially the case in the future when rapid and massive urbanization is expected (Gao & O'Neill, 2020). Additionally, combining the transient albedo scheme with the new capacity of representing urban land changes (Fang et al., 2023) in the development version of CESM could further consider the future urbanization process. In this work, we used land-only simulations to demonstrate the validity of our model development. The main goal is to develop this functionality for CESM. For our next step, we plan to conduct fully coupled simulations, particularly with the newly-developed dynamic urban capability, to examine land-atmosphere interactions under both climate change and urbanization scenarios.

In the face of uncertain urban climate risks, a transient representation of urban albedo proves beneficial for modeling flexible urban adaptive policy and practice in a realistic way. Our new scheme for incorporating transient urban surface albedo demonstrates computational efficiency, minimizing additional computational costs, as illustrated in Appendix E. This transient albedo scheme holds promise for applications beyond policy-driven adaptations, such as representing natural variations in albedo due to surface material wear and tear/weathering, pollutant deposition, or changes in vegetation cover. For instance, the albedo of green roof (Wang et al., 2021) can fluctuate with the growth cycles of vegetation and seasonal changes in leaf cover. The scheme can be adapted to model these albedo changes by customizing urban albedo adjustments in corresponding time steps. Moreover, this scheme's adaptability is not limited to urban surface albedo modifications but also facilitates incorporating additional urban parameters, such as urban surface emissivity. This expansion offers more options for representing complex urban environments without imposing substantial computational burdens.

Appendix A: Community Earth System Model–Urban (CLMU)

See Figure A1.

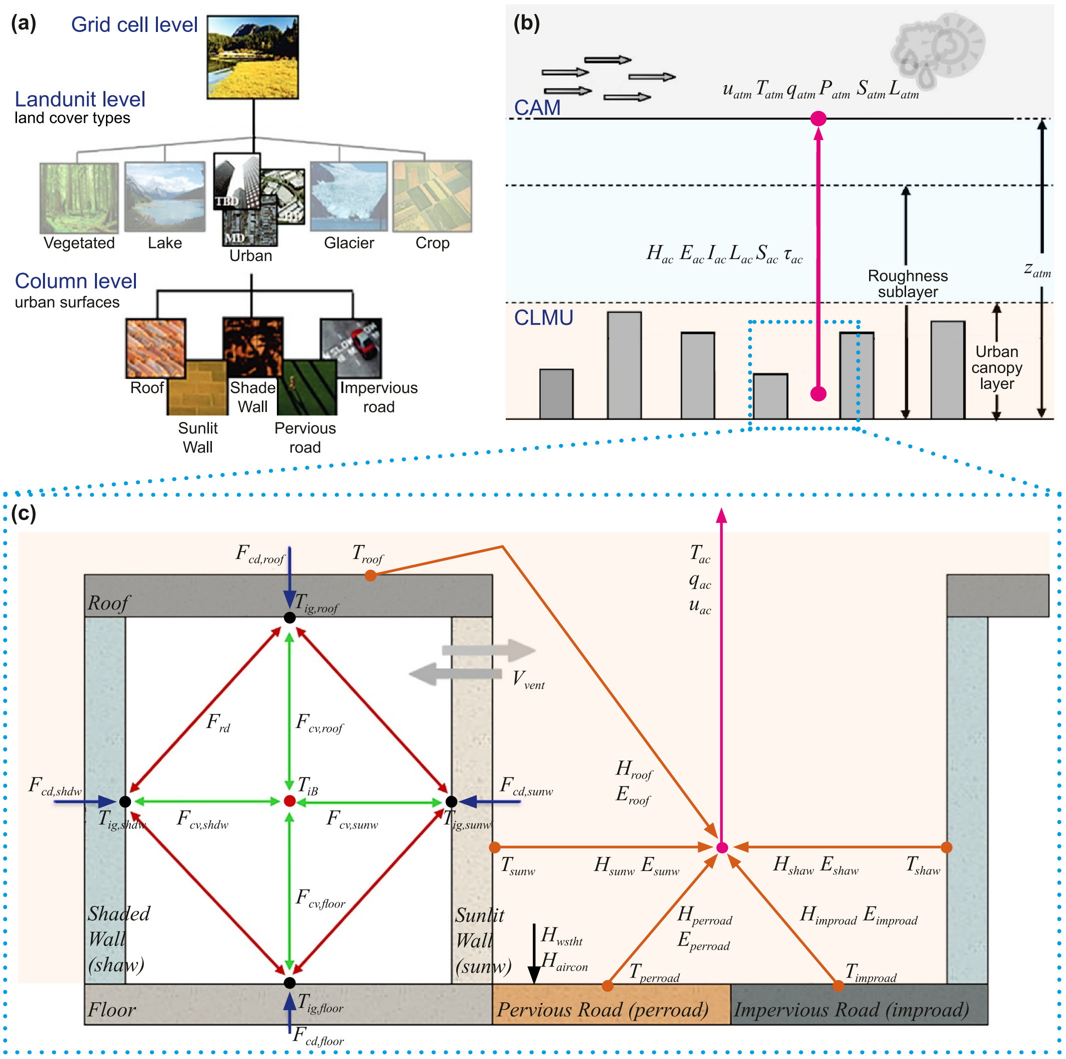

Figure A1. Urban representation and parameterization. (a) Urban surface representation hierarchy in CLM5. (b) Interactions between the atmosphere and urban canopy. CLMU is forced by the CAM at reference height z_{atm} (m). Atmospheric parameters include the atmospheric wind u_{atm} $\left(\mathrm{m\ s^{-1}}\right)$, temperature T_{atm} (K), humidity q_{atm} (kg kg^{-1}), precipitation P_{atm} $\left(\mathrm{mm\ s^{-1}}\right)$, solar radiation S_{atm} (W m^{-2}), and longwave radiation L_{atm} (W m^{-2}). The pick arrows represent the upward fluxes from the urban canopy layer to CAM, including sensible heat flux H_{ac} (W m^{-2}), water vapor flux E_{ac} $\left(\mathrm{kg\ m^{-2}\ s^{-1}}\right)$, albedo I_{ac}, emitted longwave radiation L_{ac} (W m^{-2}), absorbed short-wave S_{ac} (W m^{-2}), and momentum τ_{ac} (kg m^{-1} s^{-2}). (c) Urban energy scheme. T_{ac} is the urban canopy air temperature (K), q_{ac} the specific humidity of urban canopy layer air (kg kg^{-1}), and u_{ac} the wind speed (m s^{-1}) at the average height of the building. The orange arrows represent the heat and moisture fluxes (W m^{-2}) from the urban facets to the §urban canopy air. T_{roof}, T_{sunw}, T_{shaw}, $T_{perroad}$, and $T_{improad}$ is the surface temperature of the roof, sunlit wall, shaded wall, pervious surfaces, and impervious surfaces. H_{roof}, H_{sunw}, H_{shaw}, $H_{perroad}$, and $H_{improad}$ is the sensible heat flux on each surface. E_{roof}, E_{sunw}, E_{shaw}, $E_{perroad}$, and $E_{improad}$ is the water vapor flux. Blue arrows represent heat conduction fluxes (W m^{-2}) of the roof $F_{cd,roof}$, sunlit wall $F_{cd,sunw}$, shaded wall $F_{cd,shaw}$, and floor $F_{cd,floor}$. The red arrows represent longwave exchange F_{rd} (W m^{-2}) between the interior surfaces. Green arrows represent sensible heat transfer (W m^{-2}) between the interior surface of the building and the indoor air by $F_{cv,roof}$, $F_{cv,sunw}$, $F_{cv,shaw}$, and $F_{cv,floor}$, respectively. The black arrows represent the heat waste H_{wstht} (W m^{-2}) from heating in winter or the heat removed H_{aircon} (W m^{-2}) by air conditioning in summer. Gray arrows represent the ventilation flow rate V_{vent} $\left(\mathrm{m^3\ s^{-1}}\right)$. Source: Adapted from Oleson et al. (2013); Oleson and Feddema (2020).

Appendix B: Urban Heat Island Intensity

B1. Quantification Using CESM Outputs

At the grid level, urban heat island intensity is calculated by the contrast between grid-level urban and rural temperatures. Surface urban heat island intensity in a certain grid cell $(\mathrm{SUHII_g})$ is calculated as:

$$\mathrm{SUHII_g} = \mathrm{TG\_U_g} - \mathrm{TG\_R_g}, \tag{B1}$$

where urban and rural variables are weighted by landunit fractions within a grid cell. CLM5 represents urban areas in three types: tall building district (TBD), high density (HD), and medium density (MD). It does not represent and parameterize rural areas but outputs rural variables based on the counterpart from natural vegetation and crop fractions. The urban ground temperature in a certain grid cell $(\mathrm{TG\_U_g})$ is calculated as:

$$\mathrm{TG\_U_g} = \frac{\sum_{l=7,8,9}\mathrm{PCT\_URBAN}_{l,\mathrm{g}} \times \mathrm{TG}_{l,\mathrm{g}}}{\sum_{l=7,8,9}\mathrm{PCT\_URBAN}_{l,\mathrm{g}}}, \tag{B2}$$

and rural ground temperature $(\mathrm{TG\_R_g})$ is calculated as:

$$\mathrm{TG\_R_g} = \frac{\mathrm{PCT\_NATVEG_g} \times \mathrm{TG}_{l=1,\mathrm{g}} + \mathrm{PCT\_CROP_g} \times \mathrm{TG}_{l=2,\mathrm{g}}}{\mathrm{PCT\_NATVEG_g} + \mathrm{PCT\_CROP_g}}, \tag{B3}$$

where g indexes grid cells, l indexes landunit types where 1, 2, 7, 8, and 9 index natural vegetation, crop, TBD, HD, and MD, respectively. PCT_URBAN, PCT_NATVEG, and PCT_CROP denote the percent of urban classes, natural vegetation, and crop, respectively. At the landunit level, $\mathrm{SUHII}_{l,\mathrm{g}}$ is calculated as:

$$\mathrm{SUHII}_{l,\mathrm{g}} = \mathrm{TG\_U}_{l,\mathrm{g}} - \mathrm{TG\_R_g}, \tag{B4}$$

where l ranges from 7 to 9, presenting TBD, HD, and MD, respectively.

B2. Comparison With Observation Data

We compared the CNTL simulation results with observation to validate the baseline accuracy. The modeled annual-mean CUHII averages 0.5°C (Figure 7a) during the day and 0.9°C at night (Figure 7d), aligning with the global observation data that indicates an annual-mean daytime CUHII of 0.6°C and nighttime CUHII of 0.8°C in 366 cities (Du et al., 2021). Du et al. (2021) also found annual daytime and nighttime SUHII at 1.7°C and 1.1°C, respectively, and Peng et al. (2012) found the counterparts at 1.5°C and 1.1°C, respectively. When calculating daily SUHII as the average of daytime and nighttime values, reported values are 1.4°C (Du et al., 2021) and 1.3°C (Peng et al., 2012), higher than our modeled annual-mean daily SUHII of 1.2°C. This is due to that SUHII retrieved from remote-sensing images used skin radiative temperatures, which may not be comparable with the one based on ground temperatures simulated in CESM.

B3. Seasonal Differences

See Figure B1.

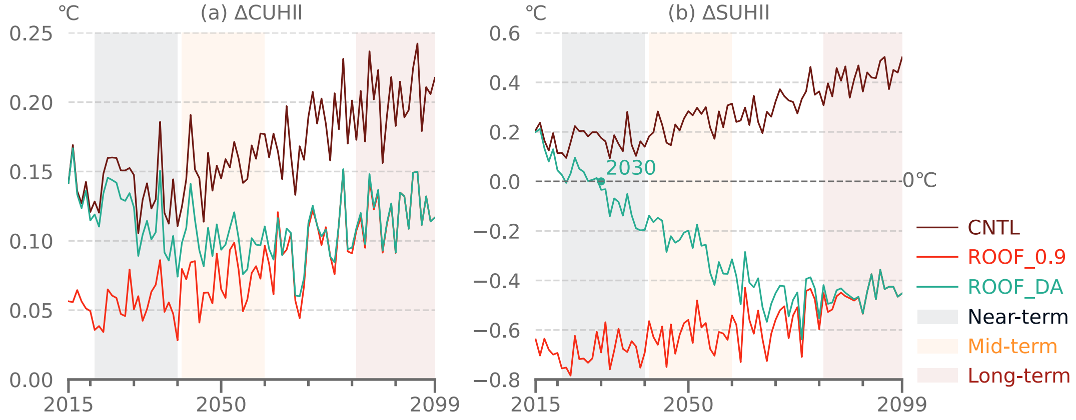

Figure B1. Differences in urban heat island intensity between JJA-mean and DJF-mean. (a) Difference in canopy urban heat island intensity (ΔCUHII). (b) Difference in surface urban heat island intensity (ΔSUHII).

Appendix C: Urban Albedo-Induced Surface Energy Changes

C1. Actual Surface Albedo

The pattern of annual-mean actual surface albedo (α) remains consistent with the static or transient ALB_ROOF inputs (Figure C1a). The difference between DJF-mean and JJA-mean α ($\Delta\alpha$) is positive (Figure C1b), indicating that α in DJF is generally higher than in JJA, considering that snow in winter is highly reflective. $\Delta\alpha$ shows a downward trend in CNTL simulation, which results from decreasing DJF-mean α (Table C1).

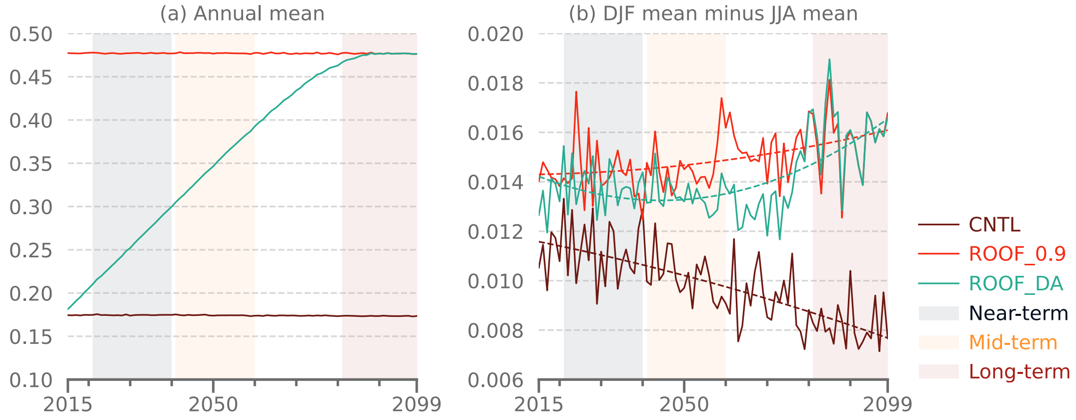

Figure C1. Actual surface albedo. (a) Annual-mean actual surface albedo α. (b) Difference ($\Delta\alpha$) between DJF-mean and JJA-mean actual surface albedo. The dashed lines represent the fitted trend obtained from the non-linear model using a quadratic function of the form $f(x) = ax^2 + bx + c$.

Table C1
Statistical Regression Between Annual-Mean Absorbed Solar Radiation and Urban Albedo Parameter (ALB_) Using the Fixed Effect Model

Simulation	ROOF_DA	ROOF_DA	ROOF_DA	IMPROAD_DA	WALL_DA	ROOF_IMPROAD_DA	ROOF_WALL_IMPROAD_DA
Variable metric	ANN	JJA	DJF	ANN	ANN	ANN	ANN
Dependent variable					FSA		
ALB_	-94.096^{***}	-105.70^{***}	-73.135^{***}	-11.370^{***}	-24.312^{***}	-105.80^{***}	-139.74^{***}
FSDS	0.7204^{***}	0.6914^{***}	0.6740^{***}	0.8050^{***}	0.7586^{***}	0.6957^{***}	0.5962^{***}
Constant	46.611^{***}	58.817^{***}	41.927^{***}	7.2874^{***}	19.487^{***}	54.754^{***}	84.352^{***}

Table C1
Continued

Simulation Variable metric	ROOF_DA ANN	ROOF_DA JJA	ROOF_DA DJF	IMPROAD_DA ANN	WALL_DA ANN	ROOF_IMPROAD_DA ANN	ROOF_WALL_IMPROAD_DA ANN
Number of grid cells with urban fraction					3,538		
Adjusted r^2	0.866	0.857	0.732	0.926	0.898	0.887	0.932

Note. ANN denotes the annual mean, JJA denotes the June–July–August mean, and DJF denotes the December–January–February mean. *** denotes the 0.01 significance level.

C2. Vertical Sections Illustrating Reflection of Solar Radiation Within the Canyon

See Figures C2 and C3.

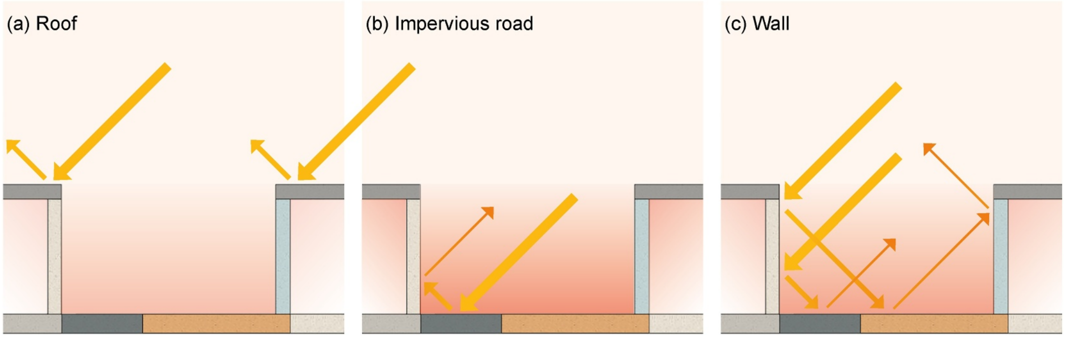

Figure C2. Reflectivity over urban surfaces. (a) Roof. (b) Impervious road. (c) Wall.

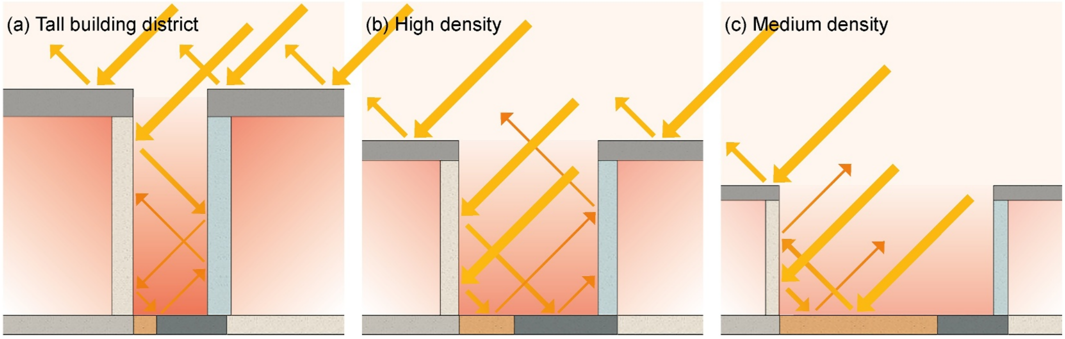

Figure C3. Reflectivity over urban landunits. (a) Tall building district (TBD). (b) High density (HD). (c) Medium density (MD).

C3. Surface Energy Changes by Albedo Modification

See Figure C4.

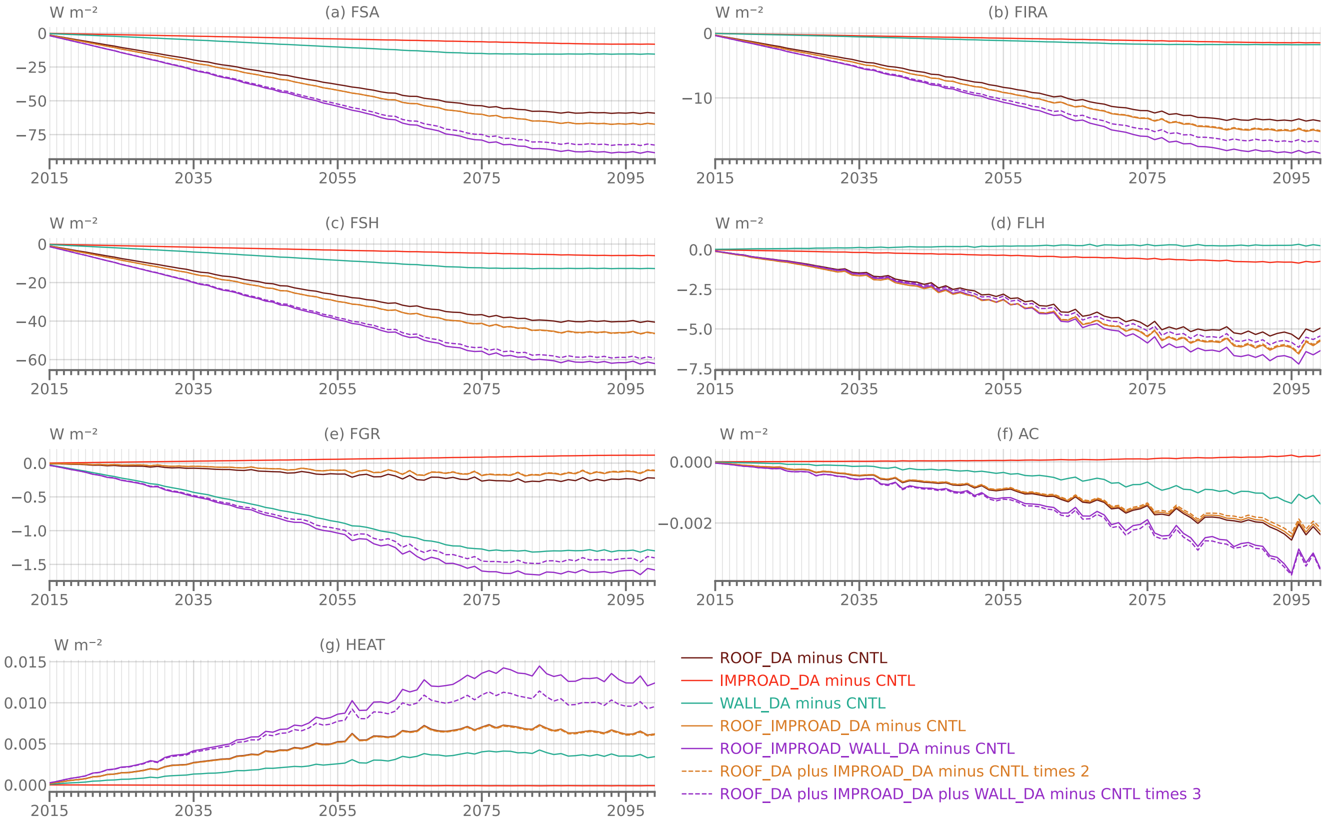

Figure C4. Urban heat flux changes induced by transient urban albedo. (a) Absorbed solar radiation (FSA). (b) Net longwave radiation (FIRA). (c) Sensible heat flux (FSA). (d) Latent heat flux (FLH). (e) Ground heat flux (FGR). (f) Air conditioning flux (AC). (g) Building space heating flux (HEAT).

Appendix D: Atmospheric Variables

This study uses atmosphere data from the BSSP370cmip6 simulations. As shown in the period 2015–2099 (Figure D1), the annual-mean TBOT jumps from 18.2°C in 2015 to 18.9°C in 2050 and 21.7°C in 2099. Seasonally, in the June–July–August (JJA) period, TBOT reaches 27.2°C in 2099, 3.1°C and 3.8°C higher than in

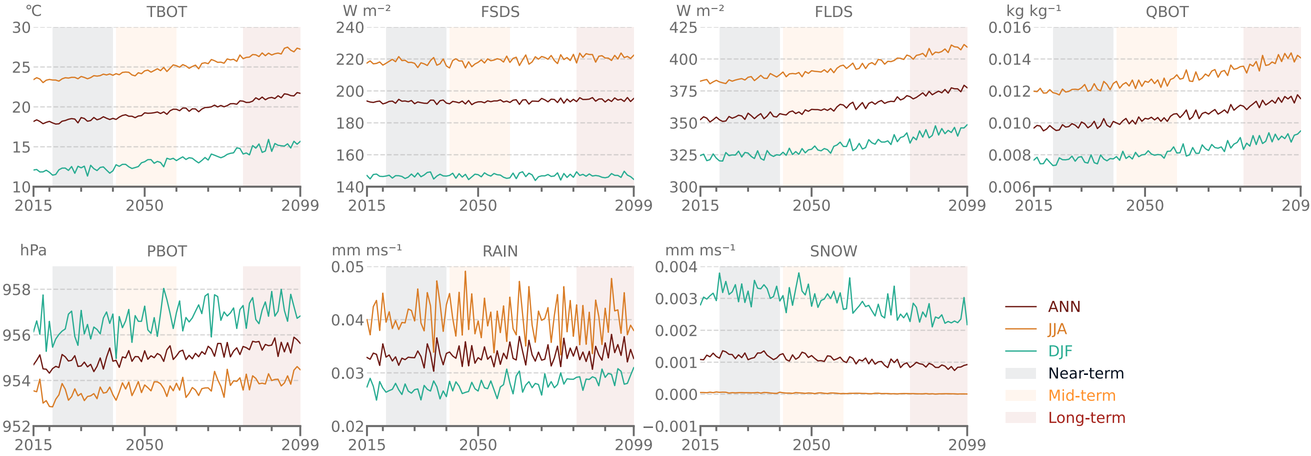

Figure D1. Period (2015–2099) of atmospheric variables under the SSP3-7.0 scenario. Atmospheric variables are calculated for annual-mean, June–July–August (JJA) mean, and December–January–February (DJF) mean. TBOT is the atmospheric air temperature (°C). FSDS is the atmospheric incident solar radiation $\left(\mathrm{W\ m^{-2}}\right)$. FLDS is the longwave radiation $\left(\mathrm{W\ m^{-2}}\right)$. QBOT is the specific humidity $\left(\mathrm{kg\ kg^{-1}}\right)$. PBOT is the surface pressure (hPa). RAIN is the rain $\left(\mathrm{mm\ ms^{-1}}\right)$. SNOW is the snow $\left(\mathrm{mm\ ms^{-1}}\right)$.

2050 and 2015, respectively. In the December–January–February (DJF) period, TBOT shows a 3.2°C increase over 85 years. FLDS and QBOT show a similar trend of accelerating growth as TBOT. FSDS and PBOT fluctuate moderately while rainfall displays intensive changes, particularly in summer. Alongside warming, snowfall generally reduces.

Appendix E: Workflow Profiling

We used the UK National Supercomputing Service named ARCHER2 (https://docs.archer2.ac.uk) to evaluate the computational performance of the transient urban albedo scheme in CESM2.1.4. In ARCHER2, each computer node has 128 cores as dual AMD EPYC 7742 64-core 2.25GHz processing elements (PEs). The compiler is the GNU Compiler Collection, the MPI library is MPICH, and the model driver is CPL7. The component set includes a data atmosphere component (DATM), active land component (CLM5), and active river runoff component (MOSART) with other stub components such as glacier (GLC), sea-ice (ICE), surface wave (WAV), and ocean (OCN). We evaluated the computational performance of the new scheme from two aspects: workflow and cost.

Based on a single node of 128 cores, we compared workflows using default and transient schemes through 3-year simulations during 2015–2018. A conventional approach with the default scheme needed to manually resubmit case by case to realize albedo input varying by time (Figure E1a). Using the transient urban albedo scheme read in data streams without interruptions, where the simulation took 0.8min for initialization, 79.2min for job running, and 0.5min for output archive (Figure E1b). Both the conventional approach and stream approach cost similar computing resources of 56.2–56.7pe-hrs/simulated_year, whose final outputs are almost the same.

To examine computational cost, we ran land-only simulations with a grid spacing of 0.9375° latitude by 1.25° longitude for 20 years from 2015 to 2035. We set several task configurations: single (1 node/128 total PEs), small (4 nodes/12 total PEs, and 6 nodes/768 total PEs), medium (8 nodes/1,024 total PEs), large (12 nodes/1,536 total PEs), and heavy (16 nodes/2048 total PEs) task counts. Each configuration ran two simulations: one used the default scheme ("Dynamic_UrbanAlbedoRoof = .false.") and the other used the transient urban albedo scheme ("Dynamic_UrbanAlbedoRoof = .true."). The major difference between the two schemes was the land model process, where the machine read and calculated roof albedo whether by constant parameters or data streams. The simulation timing was recorded through CESM's tool "getTiming".

Figure E2 shows computational cost, initialization time, and run speed. Those employing the transient urban albedo scheme closely match the default scheme in terms of computational cost and overall simulation speed. Though the overall difference is relatively minimal, the transient scheme exhibited a longer initialization period in the 1-node and 4-node simulations.

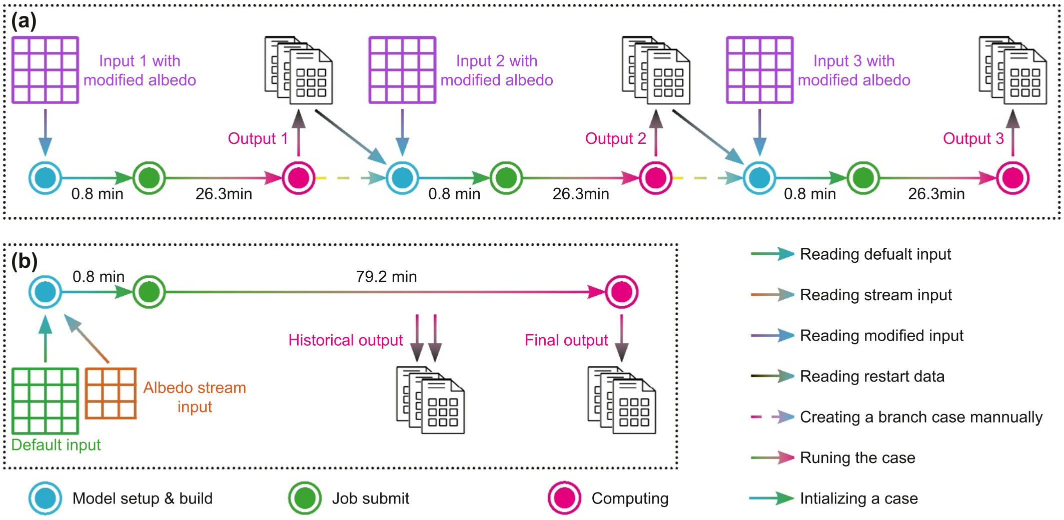

Figure E1. Workflows of implementing time-varying urban surface albedos. (a) Default scheme, (b) transient urban albedo scheme. Both simulations ran from 2015 to 2018 using 1 node/128 total PEs in the Archer2 machine.

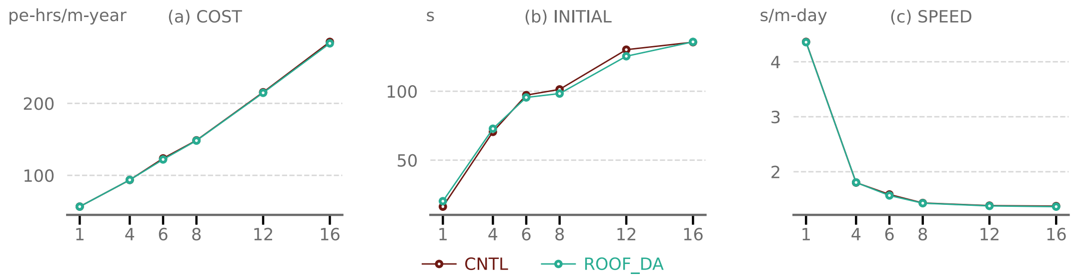

Figure E2. Profiling of different simulation workflows. (a) Computation cost (COST), measured in processing element hours per simulated year. (b) Model initialization time (INITIAL), measured in seconds. (c) Simulation running speed (SPEED), measured in seconds per simulated day.

Appendix F: Abbreviations and Acronyms

See Table F1.

Table F1
Variable Definitions

Variable name	Long name description	Unit	Data source
α	Actual urban surface albedo	unitless	Equation 12
AC*	Air conditioning flux	W m^{-2}	CLM5 outputs
AHF	Anthropogenic heat flux going into climate system	W m^{-2}	Equation 10
ALB_	Prescribed urban surface albedo parameter (i.e., ALB_ROOF_DIF, ALB_ROOF_DIR, ALB_IMPROAD_DIF, ALB_IMPROAD_DIR, ALB_WALL_DIF, and ALB_WALL_DIR)	unitless	CLM5 inputs
AT	2-m apparent temperature	°C	CLM5 outputs
CUHII	Canopy urban heat island intensity	°C	Equation 2
DI	2-m discomfort index	°C	CLM5 outputs
FGR*	Urban ground heat flux	W m^{-2}	CLM5 outputs
FIRA*	Urban net longwave radiation	W m^{-2}	CLM5 outputs
FLDS*	Atmospheric longwave radiation	W m^{-2}	CLM5 outputs
FLH	Urban latent heat flux	W m^{-2}	CLM5 outputs
FSA*	Urban absorbed solar radiation	W m^{-2}	CLM5 outputs
FSDS*	Atmospheric incident solar radiation	W m^{-2}	CLM5 outputs
FSH*	Urban sensible heat flux	W m^{-2}	CLM5 outputs
HEAT*	Building space heating	W m^{-2}	CLM5 outputs
HUMIDEX*	2-m humidity index	°C	CLM5 outputs
NWS_HI	2-m U.S. National Weather Service Heat Index	°C	CLM5 outputs
PBOT*	Atmospheric pressure at surface	Pa	CLM5 outputs
QBOT*	Atmospheric humidity	kg kg^{-1}	CLM5 outputs
RAIN*	Rain	mm s^{-1}	CLM5 outputs
SNOW*	Snow	mm s^{-1}	CLM5 outputs
SUHII	Surface urban heat island intensity	°C	Equation 1
sWBGT*	2-m simplified wet-bulb globe temperature	°C	CLM5 outputs
TBOT*	Atmospheric air temperature	°C	CLM5 outputs
TBUILD*	Indoor temperature	°C	CLM5 outputs

Table F1
Continued

Variable name	Long name description	Unit	Data source
TG_R*	Rural surface temperature	°C	CLM5 outputs
TG_U*	Urban surface temperature	°C	CLM5 outputs
TSA_R*	Rural 2-m air temperature	°C	CLM5 outputs
TSA_U*	Urban 2-m air temperature	°C	CLM5 outputs
WASTEHEAT*	Sensible heat flux from heating and cooling sources of urban waste heat	$W\ m^{-2}$	CLM5 outputs

Note. * denotes using variable names along with the corresponding CLM5 output variables.

Conflict of Interest

The authors declare no conflicts of interest relevant to this study.

Data Availability Statement

The Community Land Model version 5 (CLM5) source code is available at https://github.com/ESCOMP/CTSM (CTSM Development Team, 2022). The source code of "UrbanDynAlbMod" scheme, as well as the scripts and data to reproduce the results and figures, are available at https://github.com/envdes/code_DynamicUrbanAlbedo (Zheng & Sun, 2024).

Acknowledgments
This work used the ARCHER2 UK National Supercomputing Service (https://www.archer2.ac.uk). The authors would like to acknowledge the assistance given by Research IT and the use of the HPC Pool and Computational Shared Facility at The University of Manchester. The support of Dr. Douglas Lowe and Christopher Grave from Research IT at The University of Manchester is gratefully acknowledged. Z.Z. appreciates the support provided by the academic start-up funds from the Department of Earth and Environmental Sciences at The University of Manchester. Y.S. is supported by Z.Z's academic start-up funds. Contributions from K.W.O. are based upon work supported by the NSF National Center for Atmospheric Research, which is a major facility sponsored by the U.S. National Science Foundation under Cooperative Agreement No. 1852977. L.Z. acknowledges the support by the U.S. National Science Foundation (CAREER award Grant 2145362). We gratefully thank three anonymous reviewers for their constructive comments that substantially improved the manuscript.

References

Akbari, H., & Matthews, H. D. (2012). Global cooling updates: Reflective roofs and pavements. *Energy and Buildings*, *55*, 2–6. https://doi.org/10.1016/j.enbuild.2012.02.055

Akbari, H., Matthews, H. D., & Seto, D. (2012). The long-term effect of increasing the albedo of urban areas. *Environmental Research Letters*, *7*(2), 024004. https://doi.org/10.1088/1748-9326/7/2/024004

Akbari, H., Menon, S., & Rosenfeld, A. (2009). Global cooling: Increasing world-wide urban albedos to offset CO_2. *Climatic Change*, *94*(3–4), 275–286. https://doi.org/10.1007/s10584-008-9515-9

Bateni, S. M., & Entekhabi, D. (2012). Relative efficiency of land surface energy balance components. *Water Resources Research*, *48*(4), W04510. https://doi.org/10.1029/2011WR011357

Boriboonsomsin, K., & Reza, F. (2007). Mix design and benefit evaluation of high solar reflectance concrete for pavements. *Transportation Research Record*, *2011*(1), 11–20. https://doi.org/10.3141/2011-02

Brousse, O., Simpson, C., Zonato, A., Martilli, A., Taylor, J., Davies, M., & Heaviside, C. (2024). Cool roofs could be most effective at reducing outdoor urban temperatures in London (United Kingdom) compared with other roof top and vegetation interventions: A mesoscale urban climate modeling study. *Geophysical Research Letters*, *51*(13), e2024GL109634. https://doi.org/10.1029/2024GL109634

Buzan, J. R., Oleson, K. W., & Huber, M. (2015). Implementation and comparison of a suite of heat stress metrics within the Community Land Model version 4.5. *Geoscientific Model Development*, *8*(2), 151–170. https://doi.org/10.5194/gmd-8-151-2015

Chakraborty, T. C., Lee, X., Ermida, S., & Zhan, W. (2021). On the land emissivity assumption and Landsat-derived surface urban heat islands: A global analysis. *Remote Sensing of Environment*, *265*, 112682. https://doi.org/10.1016/j.rse.2021.112682

Chakraborty, T. C., & Qian, Y. (2024). Urbanization exacerbates continental- to regional-scale warming. *One Earth*, *7*(8), 1387–1401. https://doi.org/10.1016/j.oneear.2024.05.005

Chen, J., Zhou, Z., Wu, J., Hou, S., & Liu, M. (2019). Field and laboratory measurement of albedo and heat transfer for pavement materials. *Construction and Building Materials*, *202*, 46–57. https://doi.org/10.1016/j.conbuildmat.2019.01.028

CTSM Development Team. (2022). ESCOMP/CTSM: Add SSP3-7.0 extension, and SMYLE 1850 and transient, compsets and use-cases [Software]. *Zenodo*. https://doi.org/10.5281/zenodo.6032448

Dirmeyer, P. A., Gao, X., Zhao, M., Guo, Z., Oki, T., & Hanasaki, N. (2006). GSWP-2: Multimodel analysis and implications for our perception of the land surface. *Bulletin of the American Meteorological Society*, *87*(10), 1381–1398. https://doi.org/10.1175/BAMS-87-10-1381

Djukic, A., Vukmirovic, M., & Stankovic, S. (2016). Principles of climate sensitive urban design analysis in identification of suitable urban design proposals. Case study: Central zone of Leskovac competition. *Energy and Buildings*, *115*, 23–35. https://doi.org/10.1016/j.enbuild.2015.03.057

Du, H., Zhan, W., Liu, Z., Li, J., Li, L., Lai, J., et al. (2021). Simultaneous investigation of surface and canopy urban heat islands over global cities. *ISPRS Journal of Photogrammetry and Remote Sensing*, *181*, 67–83. https://doi.org/10.1016/j.isprsjprs.2021.09.003

Dursun, D., & Yavas, M. (2015). Climate-sensitive urban design in cold climate zone: The city of Erzurum, Turkey. *International Review for Spatial Planning and Sustainable Development*, *3*(1), 17–38. https://doi.org/10.14246/irspsd.3.1_17

Enescu, D., & Flanner, M. G. (2017). A review of thermal comfort models and indicators for indoor environments. *Renewable and Sustainable Energy Reviews*, *79*, 1353–1379. https://doi.org/10.1016/j.rser.2017.05.175

Epstein, Y., & Moran, D. S. (2006). Thermal comfort and the heat stress Indices. *Industrial Health*, *44*(3), 388–398. https://doi.org/10.2486/indhealth.44.388

Erell, E., Pearlmutter, D., Boneh, D., & Kutiel, P. B. (2014). Effect of high-albedo materials on pedestrian heat stress in urban street canyons. *Urban Climate*, *10*, 367–386. https://doi.org/10.1016/j.uclim.2013.10.005

Fang, B., Zhao, L., Oleson, K. W., Zhang, K., Lawrence, P. J., Sacks, B., et al. (2023). Representing dynamic urban land change in the Community Earth System Model (CESM). *Preprints*. https://doi.org/10.22541/essoar.168676909.95382628/v1

Flanner, M. G. (2009). Integrating anthropogenic heat flux with global climate models. *Geophysical Research Letters*, *36*(2), L02801. https://doi.org/10.1029/2008GL036465

Gao, J., & O'Neill, B. C. (2020). Mapping global urban land for the 21st century with data-driven simulations and Shared Socioeconomic Pathways. *Nature Communications*, *11*(1), 2302. https://doi.org/10.1038/s41467-020-15788-7

Georgescu, M., Morefield, P. E., Bierwagen, B. G., & Weaver, C. P. (2014). Urban adaptation can roll back warming of emerging megapolitan regions. *Proceedings of the National Academy of Sciences*, *111*(8), 2909–2914. https://doi.org/10.1073/pnas.1322280111

Guo, T., He, T., Liang, S., Roujean, J.-L., Zhou, Y., & Huang, X. (2022). Multi-decadal analysis of high-resolution albedo changes induced by urbanization over contrasted Chinese cities based on Landsat data. *Remote Sensing of Environment*, *269*, 112832. https://doi.org/10.1016/j.rse.2021.112832

Haarsma, R. J., Roberts, M. J., Vidale, P. L., Senior, C. A., Bellucci, A., Bao, Q., et al. (2016). High resolution model intercomparison project (HighResMIP v1.0) for CMIP6. *Geoscientific Model Development*, *9*(11), 4185–4208. https://doi.org/10.5194/gmd-9-4185-2016

Hertwig, D., Ng, M., Grimmond, S., Vidale, P. L., & McGuire, P. C. (2021). High-resolution global climate simulations: Representation of cities. *International Journal of Climatology*, *41*(5), 3266–3285. https://doi.org/10.1002/joc.7018

Hou, H., Su, H., Yao, C., & Wang, Z.-H. (2023). Spatiotemporal patterns of the impact of surface roughness and morphology on urban heat island. *Sustainable Cities and Society*, *92*, 104513. https://doi.org/10.1016/j.scs.2023.104513

Hou, P., Chen, Y., Qiao, W., Cao, G., Jiang, W., & Li, J. (2013). Near-surface air temperature retrieval from satellite images and influence by wetlands in urban region. *Theoretical and Applied Climatology*, *111*(1), 109–118. https://doi.org/10.1007/s00704-012-0629-7

IPCC. (2023). *Climate change 2021 – The physical science basis* (1st ed.). Cambridge University Press. https://doi.org/10.1017/9781009157896

Jackson, T. L., Feddema, J. J., Oleson, K. W., Bonan, G. B., & Bauer, J. T. (2010). Parameterization of urban characteristics for global climate modeling. *Annals of the Association of American Geographers*, *100*(4), 848–865. https://doi.org/10.1080/00045608.2010.497328

Jacobson, M. Z., & Ten Hoeve, J. E. (2012). Effects of urban surfaces and white roofs on global and regional climate. *Journal of Climate*, *25*(3), 1028–1044. https://doi.org/10.1175/JCLI-D-11-00032.1

Jamei, Y., Rajagopalan, P., & Sun, Q. C. (2019). Spatial structure of surface urban heat island and its relationship with vegetation and built-up areas in Melbourne, Australia. *Science of the Total Environment*, *659*, 1335–1351. https://doi.org/10.1016/j.scitotenv.2018.12.308

Jin, K., Wang, F., Chen, D., Liu, H., Ding, W., & Shi, S. (2019). A new global gridded anthropogenic heat flux dataset with high spatial resolution and long-term time series. *Scientific Data*, *6*(1), 139. https://doi.org/10.1038/s41597-019-0143-1

Krayenhoff, E. S., Broadbent, A. M., Zhao, L., Georgescu, M., Middel, A., Voogt, J. A., et al. (2021). Cooling hot cities: A systematic and critical review of the numerical modelling literature. *Environmental Research Letters*, *16*(5), 053007. https://doi.org/10.1088/1748-9326/abdcf1

Lawrence, D. M., Fisher, R. A., Koven, C. D., Oleson, K. W., Swenson, S. C., Bonan, G., et al. (2019). The Community Land Model version 5: Description of new features, benchmarking, and impact of forcing uncertainty. *Journal of Advances in Modeling Earth Systems*, *11*(12), 4245–4287. https://doi.org/10.1029/2018MS001583

Li, L., Bisht, G., Hao, D., & Leung, L. R. (2024). Global 1km land surface parameters for kilometer-scale Earth system modeling. *Earth System Science Data*, *16*(4), 2007–2032. https://doi.org/10.5194/essd-16-2007-2024

Li, X., Melaas, E., Carrillo, C. M., Ault, T., Richardson, A. D., Lawrence, P., et al. (2022). A comparison of land surface phenology in the northern hemisphere derived from satellite remote sensing and the Community Land Model. *Journal of Hydrometeorology*, *23*(6), 859–873. https://doi.org/10.1175/JHM-D-21-0169.1

Li, X. C., Zhao, L., Oleson, K., Zhou, Y., Qin, Y., Zhang, K., & Fang, B. (2024). Enhancing urban climate-energy modeling in the Community Earth System Model (CESM) through explicit representation of urban air-conditioning adoption. *Journal of Advances in Modeling Earth Systems*, *16*(4), e2023MS004107. https://doi.org/10.1029/2023MS004107

Liao, W., Hong, T., & Heo, Y. (2021). The effect of spatial heterogeneity in urban morphology on surface urban heat islands. *Energy and Buildings*, *244*, 111027. https://doi.org/10.1016/j.enbuild.2021.111027

Liu, Y., Chu, C., Zhang, R., Chen, S., Xu, C., Zhao, D., et al. (2024). Impacts of high-albedo urban surfaces on outdoor thermal environment across morphological contexts: A case of Tianjin, China. *Sustainable Cities and Society*, *100*, 105038. https://doi.org/10.1016/j.scs.2023.105038

Lopez-Cabeza, V. P., Alzate-Gaviria, S., Diz-Mellado, E., Rivera-Gomez, C., & Galan-Marin, C. (2022). Albedo influence on the microclimate and thermal comfort of courtyards under Mediterranean hot summer climate conditions. *Sustainable Cities and Society*, *81*, 103872. https://doi.org/10.1016/j.scs.2022.103872

Malevich, S. B., & Klink, K. (2011). Relationships between snow and the wintertime Minneapolis urban heat island. *Journal of Applied Meteorology and Climatology*, *50*(9), 1884–1894. https://doi.org/10.1175/JAMC-D-11-05.1

Masterton, J. M., & Richardson, F. (1979). Humidex: A method of quantifying human discomfort due to excessive heat and humidity (Tech. Rep.). Downsview, Ontario: Environment Canada. *Atmospheric Environment Service*.

Menon, S., Akbari, H., Mahanama, S., Sednev, I., & Levinson, R. (2010). Radiative forcing and temperature response to changes in urban albedos and associated CO_2 offsets. *Environmental Research Letters*, *5*(1), 014005. https://doi.org/10.1088/1748-9326/5/1/014005

Oke, T. R. (1987). *Boundary layer climates* (2nd ed.). Routledge. https://doi.org/10.4324/9780203407219

Oleson, K. W., Bonan, G. B., & Feddema, J. (2010a). Effects of white roofs on urban temperature in a global climate model. *Geophysical Research Letters*, *37*(3), L03701. https://doi.org/10.1029/2009GL042194

Oleson, K. W., Bonan, G. B., Feddema, J., & Vertenstein, M. (2008). An urban parameterization for a global climate model. Part II: Sensitivity to input parameters and the simulated urban heat island in offline simulations. *Journal of Applied Meteorology and Climatology*, *47*(4), 1061–1076. https://doi.org/10.1175/2007JAMC1598.1

Oleson, K. W., Bonan, G. B., Feddema, J. J., Vertenstein, M., & Kluzek, E. (2010b). *Technical description of an urban parameterization for the Community Land Model (CLMU) (Tech. Rep.)*. University Corporation for Atmospheric Research.

Oleson, K. W., & Feddema, J. (2020). Parameterization and surface data improvements and new capabilities for the community land model urban (CLMU). *Journal of Advances in Modeling Earth Systems*, *12*(2), e2018MS001586. https://doi.org/10.1029/2018MS001586

Oleson, K. W., Lawrence, D. M., Bonan, G. B., Drewniak, B., Huang, M., Levis, S., et al. (2013). Technical description of version 4.5 of the Community Land Model (CLM) (Tech. Rep.). *National Center for Atmospheric Research*.

Oleson, K. W., Monaghan, A., Wilhelmi, O., Barlage, M., Brunsell, N., Feddema, J., et al. (2015). Interactions between urbanization, heat stress, and climate change. *Climatic Change*, *129*(3), 525–541. https://doi.org/10.1007/s10584-013-0936-8

Oliveira, J. T., Hagishima, A., & Tanimoto, J. (2009). Estimation of passive cooling efficiency for environmental design in Brazil. *Energy and Buildings*, *41*(8), 809–813. https://doi.org/10.1016/j.enbuild.2009.02.006

Ouyang, Z., Sciusco, P., Jiao, T., Feron, S., Lei, C., Li, F., et al. (2022). Albedo changes caused by future urbanization contribute to global warming. *Nature Communications*, *13*(1), 3800. https://doi.org/10.1038/s41467-022-31558-z

Peng, S., Piao, S., Ciais, P., Friedlingstein, P., Ottle, C., Bréon, F.-M., et al. (2012). Surface urban heat island across 419 global big cities. *Environmental Science & Technology*, *46*(2), 696–703. https://doi.org/10.1021/es2030438

Riahi, K., van Vuuren, D. P., Kriegler, E., Edmonds, J., O'Neill, B. C., Fujimori, S., et al. (2017). The Shared Socioeconomic Pathways and their energy, land use, and greenhouse gas emissions implications: An overview. *Global Environmental Change*, *42*, 153–168. https://doi.org/10.1016/j.gloenvcha.2016.05.009

Salvati, A., Kolokotroni, M., Kotopouleas, A., Watkins, R., Giridharan, R., & Nikolopoulou, M. (2022). Impact of reflective materials on urban canyon albedo, outdoor and indoor microclimates. *Building and Environment*, *207*, 108459. https://doi.org/10.1016/j.buildenv.2021.108459

Santamouris, M., Cartalis, C., Synnefa, A., & Kolokotsa, D. (2015). On the impact of urban heat island and global warming on the power demand and electricity consumption of buildings—A review. *Energy and Buildings*, *98*, 119–124. https://doi.org/10.1016/j.enbuild.2014.09.052

Santamouris, M., & Fiorito, F. (2021). On the impact of modified urban albedo on ambient temperature and heat related mortality. *Solar Energy*, *216*, 493–507. https://doi.org/10.1016/j.solener.2021.01.031

Santamouris, M., Synnefa, A., & Karlessi, T. (2011). Using advanced cool materials in the urban built environment to mitigate heat islands and improve thermal comfort conditions. *Solar Energy*, *85*(12), 3085–3102. https://doi.org/10.1016/j.solener.2010.12.023

Schär, C., Fuhrer, O., Arteaga, A., Ban, N., Charpilloz, C., Di Girolamo, S., & Wernli, H. (2021). Prospects for kilometer-scale climate models. *Bulletin of the American Meteorological Society*, *102*(1), 47–52. https://doi.org/10.1175/BAMS-D-18-0167.1

Schatz, J., & Kucharik, C. J. (2014). Seasonality of the urban heat island effect in Madison, Wisconsin. *Journal of Applied Meteorology and Climatology*, *53*(10), 2371–2386. https://doi.org/10.1175/JAMC-D-14-0107.1

Schlaerth, H. L., Silva, S. J., Li, Y., & Li, D. (2023). Albedo as a competing warming effect of urban greening. *Journal of Geophysical Research: Atmospheres*, *128*(24), e2023JD038764. https://doi.org/10.1029/2023JD038764

Schultz, N. M., Lee, X., Lawrence, P. J., Lawrence, D. M., & Zhao, L. (2016). Assessing the use of subgrid land model output to study impacts of land cover change. *Journal of Geophysical Research: Atmospheres*, *121*(11), 6133–6147. https://doi.org/10.1002/2016JD025094

Senevirathne, D. M., Jayasooriya, V. M., Dassanayake, S. M., & Muthukumaran, S. (2021). Effects of pavement texture and colour on urban heat islands: An experimental study in tropical climate. *Urban Climate*, *40*, 101024. https://doi.org/10.1016/j.uclim.2021.101024

Sharma, M., Whaley, M., Chamberlain, J., Oswald, T., Schroden, R., Graham, A., et al. (2017). Evaluation of thermochromic elastomeric roof coatings for low-slope roofs. *Energy and Buildings*, *155*, 459–466. https://doi.org/10.1016/j.enbuild.2017.09.030

Smith, I. A., Fabian, M. P., & Hutyra, L. R. (2023). Urban green space and albedo impacts on surface temperature across seven United States cities. *Science of The Total Environment*, *857*, 159663. https://doi.org/10.1016/j.scitotenv.2022.159663

Steadman, R. G. (1979). The assessment of sultriness. Part I: A temperature-humidity index based on human physiology and clothing science. *Journal of Applied Meteorology*, *18*(7), 861–873. https://doi.org/10.1175/1520-0450(1979)018<0861:TAOSPI>2.0.CO;2

Steadman, R. G. (1994). Norms of apparent temperature in Australia. *Australian Meteorological Magazine*, *43*, 1–16.

Stull, R. (2011). Wet-bulb temperature from relative humidity and air temperature. *Journal of Applied Meteorology and Climatology*, *50*(11), 2267–2269. https://doi.org/10.1175/JAMC-D-11-0143.1

Tuholske, C., Caylor, K., Funk, C., Verdin, A., Sweeney, S., Grace, K., et al. (2021). Global urban population exposure to extreme heat. *Proceedings of the National Academy of Sciences*, *118*(41), e2024792118. https://doi.org/10.1073/pnas.2024792118

Ünal, Y. S., Sonuç, C. Y., Incecik, S., Topcu, H. S., Diren-Üstün, D. H., & Temizöz, H. P. (2020). Investigating urban heat island intensity in Istanbul. *Theoretical and Applied Climatology*, *139*(1), 175–190. https://doi.org/10.1007/s00704-019-02953-2

Wang, L., Huang, M., & Li, D. (2021). Strong influence of convective heat transfer efficiency on the cooling benefits of green roof irrigation. *Environmental Research Letters*, *16*(8), 084062. https://doi.org/10.1088/1748-9326/ac18ea

Wang, L., Sun, T., Zhou, W., Liu, M., Li, D., Tarasova, M. A., & Stepanenko, V. M. (2023). Deciphering the sensitivity of urban canopy air temperature to anthropogenic heat flux with a forcing-feedback framework. *Environmental Research Letters*, *18*(9), 094005. https://doi.org/10.1088/1748-9326/ace7e0

Willett, K. M., & Sherwood, S. (2012). Exceedance of heat index thresholds for 15 regions under a warming climate using the wet-bulb globe temperature. *International Journal of Climatology*, *32*(2), 161–177. https://doi.org/10.1002/joc.2257

Wu, S., Lin, X., Bian, Z., Lipson, M., Lafortezza, R., Liu, Q., et al. (2024). Satellite observations reveal a decreasing albedo trend of global cities over the past 35 years. *Remote Sensing of Environment*, *303*, 114003. https://doi.org/10.1016/j.rse.2024.114003

Xu, X., Swei, O., Xu, L., Schlosser, C. A., Gregory, J., & Kirchain, R. (2020). Quantifying location-specific impacts of pavement albedo on radiative forcing using an analytical approach. *Environmental Science & Technology*, *54*(4), 2411–2421. https://doi.org/10.1021/acs.est.9b04556

Yang, J., Wang, Z., & Kaloush, K. E. (2015). Environmental impacts of reflective materials: Is high albedo a 'silver bullet' for mitigating urban heat island? *Renewable and Sustainable Energy Reviews*, *47*, 830–843. https://doi.org/10.1016/j.rser.2015.03.092

Yang, P., Ren, G., & Liu, W. (2013). Spatial and temporal characteristics of Beijing urban heat island intensity. *Journal of Applied Meteorology and Climatology*, *52*(8), 1803–1816. https://doi.org/10.1175/JAMC-D-12-0125.1

Yao, R., Wang, L., Huang, X., Liu, Y., Niu, Z., Wang, S., & Wang, L. (2021). Long-term trends of surface and canopy layer urban heat island intensity in 272 cities in the mainland of China. *Science of The Total Environment*, *772*, 145607. https://doi.org/10.1016/j.scitotenv.2021.145607

Ye, X., Luo, Y., Gao, X., & Zhu, S. (2012). Design and evaluation of a thermochromic roof system for energy saving based on poly(N-isopropylacrylamide) aqueous solution. *Energy and Buildings*, *48*, 175–179. https://doi.org/10.1016/j.enbuild.2012.01.024

Yu, W., Mengersen, K., Wang, X., Ye, X., Guo, Y., Pan, X., & Tong, S. (2012). Daily average temperature and mortality among the elderly: A meta-analysis and systematic review of epidemiological evidence. *International Journal of Biometeorology*, *56*(4), 569–581. https://doi.org/10.1007/s00484-011-0497-3

Zeng, P., Zong, C., Duan, Z., & Wei, X. (2023). Exploring the spatial interplay between built-up environments and surface urban heat island phenomena in the main urban area of Shanghai. *Energy and Buildings*, *301*, 113739. https://doi.org/10.1016/j.enbuild.2023.113739

Zhang, J., Zhang, K., Liu, J., & Ban-Weiss, G. (2016). Revisiting the climate impacts of cool roofs around the globe using an Earth system model. *Environmental Research Letters*, *11*(8), 084014. https://doi.org/10.1088/1748-9326/11/8/084014

Zhao, L., Lee, X., & Schultz, N. M. (2017). A wedge strategy for mitigation of urban warming in future climate scenarios. *Atmospheric Chemistry and Physics*, *17*(14), 9067–9080. https://doi.org/10.5194/acp-17-9067-2017

Zhao, L., Lee, X., Smith, R. B., & Oleson, K. (2014). Strong contributions of local background climate to urban heat islands. *Nature*, *511*(7508), 216–219. https://doi.org/10.1038/nature13462

Zhao, L., Oleson, K., Bou-Zeid, E., Krayenhoff, E. S., Bray, A., Zhu, Q., et al. (2021). Global multi-model projections of local urban climates. *Nature Climate Change*, *11*(2), 152–157. https://doi.org/10.1038/s41558-020-00958-8

Zheng, Z., & Sun, Y. (2024). envdes/code_DynamicUrbanAlbedo: First Release by envdes [Software]. *Zenodo*. https://doi.org/10.5281/ZENODO.10903399

Zheng, Z., Zhao, L., & Oleson, K. W. (2021). Large model structural uncertainty in global projections of urban heat waves. *Nature Communications*, *12*(1), 3736. https://doi.org/10.1038/s41467-021-24113-9